Unique territorial and compartmental organization of chromosomes in the holocentric silkworm

Gil Jr., J.[1#], Navarrete, E.[2,3,4#], Hockens C.[5], Chowdhury, N.[3,4], Abraham, S.[3,4], Cornilleau, G.[1], Lei, E.P.[6], Mozziconacci, J.[7], Banigan, E.J.[3,4], Rosin, L.F.[5], Mirny, L.A.[3,4,1]*, Muller, H.[1]*, Drinnenberg, I.A.[1]*

Affiliations:
1 Institut Curie, PSL University, Sorbonne Université, CNRS, Nuclear Dynamics, 75005 Paris, France
2 Department of Biology, Massachusetts Institute of Technology, Cambridge, MA 02139, USA
3 Institute for Medical Engineering and Science, Massachusetts Institute of Technology, Cambridge, MA 02139, USA
4 Department of Physics, Massachusetts Institute of Technology, Cambridge, MA 02139, USA
5 Unit on Chromosome Dynamics, Division of Developmental Biology, *Eunice Kennedy Shriver* National Institute of Child Health and Human Development, National Institutes of Health, Bethesda, MD 20892 USA
6 Nuclear Organization and Gene Expression Section; Laboratory of Biochemistry and Genetics, National Institute of Diabetes and Digestive and Kidney Diseases, National Institutes of Health, Bethesda, MD 20892 USA
7 StrInG Lab, Museum National d'Histoire Naturelle, Paris, France

[#] These authors contributed equally to the work

*Correspondence: leonid@mit.edu (L. Mirny), heloise.muller@curie.fr (H. Muller), ines.drinnenberg@curie.fr (I. Drinnenberg)

Abstract

Hallmarks of multicellular eukaryotic genome organization are chromosome territories, compartments, and loop-extrusion-mediated structures, including TADs. However, these are mainly observed in model organisms, and most eukaryotes remain unexplored. Using Hi-C in the silkworm *Bombyx mori* we discover a novel chromatin folding structure, compartment S, which is "secluded" from the rest of the chromosome. This compartment exhibits loop extrusion features and a unique genetic and epigenetic landscape, and it localizes towards the periphery of chromosome territories. While euchromatin and heterochromatin display preferential compartmental contacts, S domains are remarkably devoid of contacts with other regions, including with other S domains. Polymer simulations show that this contact pattern can only be explained by high loop-extrusion activity within compartment S, combined with low extrusion elsewhere through the genome. This unique, targeted extrusion represents a novel phenomenon and underscores how evolutionarily conserved mechanisms—compartmentalization and loop extrusion—can be repurposed to create new 3D genome architectures.

Introduction

Three-dimensional (3D) genome organization regulates cellular physiology by influencing gene expression [1–8], DNA replication [9,10], and DNA repair [11,12], among other processes [8,13–16]. This rich, multiscale spatial organization includes chromosome territories (CTs) [17–19], chromatin compartments [20,21], and extrusion-mediated loops [22–29], each of which arises through a distinct physical mechanism [13,16,30]. These mechanisms simultaneously act on chromatin, raising the possibility that they may interact with each other. Here, we study the genome folding of the silkworm *Bombyx mori* and uncover a novel interplay between two major mechanisms: compartmentalization and loop extrusion.

Chromatin compartmentalization is thought to arise from affinity-mediated phase separation of different types of chromatin. By this mechanism, similar types of chromatin (broadly, euchromatin and heterochromatin) may segregate into spatially distinct compartments [13,30–33]. In Hi-C and other chromatin contact maps, this effect manifests as a distinctive checkerboarding pattern reflecting preferential interactions between segments of like chromatin state. Studies suggest that compartmentalization maintains epigenetic state, through maintaining its long-term memory [34,35] and the co-regulation of epigenetic states between distal loci [36].

Loop extrusion is driven by molecular motors belonging to the structural maintenance of chromosome (SMC) complexes, such as cohesin and condensin. These motors bind to chromatin and extrude it into progressively enlarging loops. Cohesin extrudes chromatin and is stalled by barriers, such as CTCF in vertebrates. This process forms TADs in Hi-C maps, which are insulated domains of enriched contacts, as well as dots and stripes [24,25,37–41]. In vertebrates, the interphase genome is typically fully partitioned into TADs, reflecting a relatively uniform distribution of cohesins across the genome. However, in certain developmental contexts, cohesin can be recruited to specific loci and form a distinct Hi-C contact pattern, termed fountains/jets/plumes [42–47]. Thus, loop extrusion activity may generate different structures depending on cohesin loading patterns and the presence of extrusion barriers in the surrounding chromatin.

Studies of extrusion in vertebrate systems have often found an antagonistic relationship between loop extrusion and compartmentalization [26,27,48–50]. Suppressing cohesin activity removes chromatin loops and weakens TADs, while also strengthening compartments [26,27,48,49]. Increasing cohesin activity by extending its residence time lengthens chromatin loops, strengthens TADs, and weakens compartments [48–50]. Polymer modeling reveals this antagonism may be caused by cohesin bridging interactions between different types of compartments and increasing chromatin mobility [32]. However, a recent study demonstrated that loop extrusion is not solely antagonistic to compartmentalization, as stabilized extrusion enhances certain compartments in simulations of mitotic chromosomes [51]. Thus, the effect of loop extrusion on compartmentalization may depend on the precise activity of loop extrusion in a given context.

While many studies focus on loop extrusion in vertebrates, loop extrusion is well conserved across the kingdoms of life. Indeed, many important insights into vertebrate loop extrusion activity were first established in other organisms. For example, observations of SMC complexes in yeast [52–55] and bacteria [56,57] were foundational for subsequent studies explaining the nature of SMC-RNA Polymerase interactions in mammals [58,59]. Similarly, targeted loading of SMC complexes to specific loci in bacteria [60–63] preceded the discovery of

96 fountains/jets/plumes in vertebrate cells [42,43,46]. Therefore, studying diverse organisms
97 beyond vertebrates can reveal new principles of loop extrusion and genome organization.
98 While a recent study of 3D genomics compared a diverse set of organisms, it excluded
99 species with radically different linear chromosome organization, such as species with
100 holocentric chromosomes [64]. These have centromeric function distributed along the entire
101 length of each chromosome, unlike most eukaryotes that have a single centromeric region per
102 chromosome. Few studies have investigated the 3D genome organization of holocentric
103 organisms, with the notable exception of *C. elegans* [65–68]. Thus, studies of such organisms
104 could expand our understanding of the principles of genome architecture.
105 To this end, we characterize the genome architecture of the holocentric silkworm *B.*
106 *mori*, which evolved holocentricity convergently with *C. elegans*. By combining Hi-C,
107 epigenetic and transcriptomic profiling, polymer modeling, and Oligopaint FISH, we find a
108 unique genome organization in *B. mori*. This organism exhibits a high degree of chromosome
109 territoriality, three epigenetically distinct compartments, and a nonuniform pattern of loop
110 extrusion activity. Further, we uncover an extreme instance of loop extrusion interfering with
111 compartmentalization. Our analysis and modeling demonstrate that, through targeted loop
112 extrusion, *B. mori* establishes novel, secluded domains that are depleted in chromosome-wide
113 compartment contacts. This unique chromatin structure relies on the interplay of extrusion
114 and compartmentalization and cannot arise by either mechanism alone. Our study thus
115 demonstrates how novel chromatin structures can emerge from new combinations of
116 conserved genome folding mechanisms.
117
118 **Results**

119 *Bombyx mori linear genome organization*

120 The *B. mori* genome encompasses 27 autosomes, the Z sex chromosome (Chr01), and
121 the W sex chromosome, which vary in length from approximately 8 to 22 Mb. Genome-wide
122 analysis of GC content revealed a tripartite organization of *B. mori* chromosomes, with a
123 central GC-poor region and two large telomere-proximal GC-rich regions (Figure 1A). This
124 linear organization is reminiscent of that of the nematode *C. elegans* (Figure 1B), another
125 holocentric organism whose chromosomes are divided into centers and arms [69]. We thus used
126 our GC content track along *B. mori* chromosomes to define arms and center regions for each
127 chromosome (see M&M for detail, Table S1). In *C. elegans*, chromosomal arms are enriched
128 in repetitive DNA, while centers are enriched in genes [69] (Figure 1B). In *B. mori*, we found a
129 similar organization with significant, but less distinct, patterns of transposable elements (TEs)
130 and gene coverage (Figure 1B). The similarity in linear genome organization between these
131 two species might reflect convergent evolution between the two holocentric lineages that
132 evolved independently from different monocentric ancestors [70,71].
133
134 *Chromosomes in B. mori embryos form highly segregated territories*

135 We generated Hi-C datasets from whole *B. mori* embryos at three different embryonic
136 post diapause time points (2, 24, and 48 hours after diapause release) and one adult stage
137 from the p50 reference strain. For most of our analysis, we focused on the 24-hour post-
138 diapause timepoint (PD-D2) (Figure 1C), for which we confirmed that a proportion of cells have
139 re-entered the cell cycle and are thus no longer arrested in G2 (Figure S1) [72].

140 The PD-D2 Hi-C contact pattern across all 28 chromosomes revealed very sparse inter-
141 chromosomal contacts (Figure 1D). This is consistent with recent DNA FISH data that revealed
142 that *B. mori* chromosomes are tightly folded and occupy distinct CTs [73]. Despite the similarity
143 in linear genome organization between *B. mori* and *C. elegans*, clustering between centers
144 and arms of different chromosomes, easily seen on *C. elegans* contact maps [65,66], is not evident
145 in *B. mori*. Nevertheless, drawing the average *trans* contact matrix reveals enrichments
146 between large sub-telomeric regions, indicating some degree of telomere or arm clustering
147 between chromosomes in *B. mori* (Figure 1E).
148 Despite the sparsity of inter-chromosomal contacts, we tested whether known
149 patterns of sub-nuclear positioning of chromosomes seen in other organisms are present in
150 *B. mori*. In humans, small, gene-rich chromosomes have been shown to preferentially interact
151 with each other and localize more centrally within the nucleus [20,74–76]. A length-dependent
152 contact preference can also be identified among *B. mori* chromosomes, with a group of small
153 chromosomes (Chr02, 28, 26, 20, and 16) having the highest average inter-chromosomal
154 contact frequency (Figures 1F, S2A). However, the correlation between inter-chromosomal
155 contacts and gene density is mild (Figure S2B). This might be due to the lower variation in
156 length and gene content among *B. mori* chromosomes compared to human chromosomes.
157 We also noticed a positive correlation between inter-chromosomal contacts and GC content
158 (Figure S2C), but whether GC content contributes to observed contact preferences is unclear.
159 Our data reveal conserved principles in chromosome organization in *B. mori*, such as
160 the formation of CTs and mild length-dependent inter-chromosomal contact preferences. In
161 contrast to other organisms, however, inter-chromosomal contacts are not correlated with
162 gene density, and *B. mori* chromosomes make very limited inter-chromosomal contacts
163 overall, highlighting the remarkably strong CTs in this organism.
164
165 *B. mori chromosomes are organized in three chromatin compartments*

166 We next investigated compartmentalization of *B. mori* chromosomes. Many regions of
167 the Hi-C maps displayed a characteristic checkerboard pattern of alternating regions of two
168 types, displaying enriched homotypic (self-to-self) and depleted heterotypic (self-to-other)
169 contacts (Figure 2A, left and middle panels), seen in all other animals [8,30,77–81]. However, unlike
170 Hi-C maps from any other organism, we unexpectedly found large chromatin segments that
171 do not display checkerboard patterning. Instead, these regions engage in a high degree of
172 short-range contacts but few long-range contacts with any other chromosomal segments
173 (Figure 2A, left and right panels). Therefore, these regions are atypical for compartments, but
174 also appear to be different from TADs, which are described in vertebrates and exist within
175 checkerboarding compartments.
176 To identify which chromosomal loci engage in this novel interaction pattern, we
177 applied an approach similar to a recently developed sub-compartment detection algorithm [82].
178 From the *cis* Hi-C maps, we k-means clustered the leading principal components of the
179 Pearson-correlated matrices, revealing groups of loci with similar contact profiles (Figures 2A,
180 and Table S2). This strategy enabled us to define three main clusters along each chromosome,
181 which we then unified across the genome based on epigenetic composition (Materials and
182 Methods).
183 We profiled active (H3K36me3, H3K4me3) and silent (H3K27me3, H3K9me3) histone
184 marks by ChIP-seq in the PD-D2 embryonic stage of *B. mori*. We also included H2A.Z, a histone

185 variant associated with transcriptional control [83], which is enriched in a sub-compartment that
186 shows an attenuated checkerboarding pattern in the cancer cell line HCT116 [82]. Additionally,
187 we included H4K20me1, a mark associated with centromeric nucleosomes in vertebrates [84],
188 as well as a variety of processes including transcriptional regulation, chromosome replication
189 and segregation, DNA damage response, and chromosome compaction [85,86].
190 Consistent with the compartmentalization of euchromatin and heterochromatin
191 observed in other animals, we found that the two checkerboarding clusters were enriched in
192 active ("compartment A") and inactive ("compartment B") histone marks (Figures 2A, 2C, S3A,
193 and S3B). The third cluster captured the novel, non-checkerboarding regions. We termed this
194 cluster "compartment S," reflecting its secluded, spatially segregated behavior observed in
195 the Hi-C maps. Compartment S displayed an epigenetic signature consistent with silenced
196 chromatin, though it uniquely differed from compartment B due to its enrichment in
197 H4K20me1.
198 Domains, which we define as contiguous segments of the same compartment type, of
199 A, B, and S are heterogeneous in length and cover different fractions of the genome (Figures
200 2D, 2E). Overall, A and S domains are smaller, with a median size of 80 kb, while B domains
201 are generally larger, with a median size of 120 kb. A and B compartments cover approximately
202 50 and 30% of the genome, respectively, while S covers 15%, with 5% of the genome not
203 assigned to any of the three clusters. Consistent with our description of *B. mori* linear genome
204 organization, we found domains of compartment A are also enriched along chromosome
205 centers, while those of compartment B are enriched along the arms (Figure S3D). Domains of
206 compartment S are distributed throughout the genome, lacking preferential positioning at
207 either chromosome centers or arms (Figure S3D and S3C for the distribution of S domains).
208 We next investigated whether compartment S is distinct from compartments A and B
209 with respect to genetic features. We found that compartment S, like compartment A, has a
210 lower GC and transposable element content compared to the whole genome (Figure S3E).
211 Despite these similarities to A, compartment S corresponds to gene-poor regions and is even
212 more depleted in genes than compartment B (Figure 2F). However, unlike B, S does not appear
213 to be a repressive compartment; the expression levels of the few genes that are located within
214 S are in the range of the genome-wide distribution. Out of the 608 genes within S, about half
215 (300) are expressed at the PD-D2 stage (TPM > 10) (Figure 2G and Table S3). Gene ontology
216 analyses revealed genes within S are enriched in DNA-binding and transcription regulation
217 processes (Table 1). Given that one of the largest S domains in the genome corresponds to the
218 Hox cluster, which is expressed in the PD-D2 stage, we tested for an enrichment of homeotic
219 and Polycomb group (PcG) response genes (Figure S4). Using previously published datasets
220 [87,88], we generated a list of 399 homeotic and PcG response genes in *B. mori* and assigned
221 them to A, B, or S (Table S4, Materials and Methods). We did not find an enrichment of
222 homeotic or PcG response genes in compartment S but rather in A (Table S4).
223 We conclude that *B. mori* chromosomes segregate into three chromatin
224 compartments. In addition to the well-conserved compartments A and B, *B. mori*
225 chromosomes contain a third compartment type, compartment S, which has an
226 unprecedented pattern of contact. S exhibits a unique epigenetic landscape and covers about
227 one-sixth of the *B. mori* genome at the PD-D2 time point. While S largely encompasses gene-
228 poor regions, many genes located within S are transcriptionally active.
229
230 *Compartment S exhibits novel contact patterning and key evidence of loop extrusion activity*

To formalize our initially observed contact patterning for compartments A, B, and S, we calculated the average compartment contact strengths for all domains on the same chromosome. For A and B, we found enriched homotypic (A-A and B-B) and depleted heterotypic (A-B) interactions, confirming that A and B are compartmentalized (Figure 2H). Further, we found that domains of S were depleted in contacts with all other compartments. These formed smooth lanes of contact depletion, such that A-S, B-S, and S-S (other S domains) were all depleted at similar strengths (Figure 2H). In stark contrast to this finding, we found contacts for pairs of loci within the same, contiguous S domain (on-diagonal) were strongly enriched (Figure 2I). To our knowledge, this unexpected discordance between on- and off-diagonal Hi-C contacts has not been observed in other organisms, and it raises the question of whether this pattern arises from a previously undescribed mechanism.

In vertebrates, cohesin extrudes loops resulting in domains of local contact enrichment known as TADs and decreased compartmentalization [27,32,49,50]. Given both the high contact enrichment within S domains (Figure 2I) and their lack of checkerboard patterning (Figure 2A and H), we hypothesized that S domains might represent regions of high loop extrusion activity. We searched for evidence of loop extrusion activity in the PD-D2 Hi-C data. Key established indicators of this activity are (1) the shape of the contact frequency *P(s)* as a function of genomic separation *s* [19,27,48,89,90] and (2) the presence of specific Hi-C patterns, such as insulated domains, dots, and stripes, which also require extrusion barriers [24,26,27,41,91,92].

In the chromosome-wide *P(s)* curve (Figure 2J), we observe a characteristic "shoulder" of increased contacts and a corresponding peak in the log-derivative of *P(s)*, which are indicative of loop extrusion [19,27,48,89,93]. The peak in the log derivative plot represents the average loop size [48,90], which in this case is approximately 40-60 kb. We next computed these contact frequency curves separately for continuous segments of each compartment type (Figure 2J). Consistent with our hypothesis, the *P(s)* shoulder is most prominent for compartment S and indicates an average loop size of 40-60 kb. The *P(s)* curve in compartment B also suggests some loop extrusion activity, though extrusion in B is likely sparser with larger loops, as suggested by the smaller height and right-shift of the peak. Analysis of *P(s)* therefore indicates that loop extrusion is active in *B. mori* and is enriched in S domains.

In further support of loop extrusion in *B. mori*, we found many genomic regions with features of barrier-restricted extrusion (dots and stripes). By visual inspection, we often found such features nested within each other inside and at the edges of S domains (Figure 2K).

The Hi-C data strongly suggests that loop extrusion occurs on *B. mori* interphase chromosomes and that it is much more prominent in S domains. This preferential enrichment of extrusion differs from previous observations in vertebrates, which raises the mechanistic question of whether it is responsible for the nontrivial patterns of S contacts in *B. mori*.

Targeted loading of loop extruders to S domains can reproduce S compartment Hi-C features

Given the novel and stark contact pattern of compartment S (Figure 3A), we employed polymer modeling to systematically study which mechanisms underlie its formation. We sought to reproduce the following three Hi-C features that together make compartment S unique (Figure 3A): (*i*) contacts are enriched within contiguous, on-diagonal S domains (locally enriched, S_{intra}); (*ii*) each S domain is depleted in off-diagonal, compartment contacts with other S domains (distally depleted, S-S_{inter}); (*iii*) the depletion of contacts between S domains and the rest of the chromosome is homogenous (smooth lanes of contact depletion, S-S_{inter} ≈

S-A ≈ S-B). These features are the hallmarks of compartment S and have not been previously observed together or at all.

In addition to its unique loop extrusion activity, we found S exhibits a unique epigenetic composition, suggesting it may phase separate from compartments A and B. Because loop extrusion and phase separation independently drive chromatin folding, we asked which of these processes, either individually or in combination, are responsible for generating S features. We therefore tested three major classes of mechanistic models (Figure 3B). We first tested models in which chromatin organization was solely driven by phase separation. We then tested models with uniform loop extrusion and extrusion barriers at the edges of S domains, akin to loop extrusion behavior that generates TADs in vertebrates. These first two classes represent mechanisms of genome folding described in other animals. Finally, we tested models in which loop-extruding complexes preferentially accumulate in S over A and B.

We performed polymer simulations for each class of model, using simplified (chromatin) polymer chains with eight equally sized segments of A, B, and S monomers. Monomer identity was used to define compartment-specific affinity (**ϵ**) and loop extrusion properties (Figure 3B). For each class of model, we tested a wide range of A/B compartment strengths to recapitulate the A/B compartments observed in the experimental data.

Phase separation without loop extrusion

We investigated whether affinity-mediated phase separation, which drives the formation of chromatin compartments, could recapitulate the features of S. Experimental Hi-C maps revealed clear compartmentalization of A and B regions (i.e. A/B checkerboarding), whereas S lacked such compartment patterning. This led us to first ask whether S could emerge if A and B chromatin, but not S, exhibited self-affinity.

To test this in our polymer simulations, we systematically varied per-monomer homotypic affinities of A-to-A and B-to-B monomers to obtain a broad range of compartment strengths (Figure 3C). As expected, applying A-to-A and B-to-B affinities produced the desired checkerboard patterning of A and B compartments, consistent with their phase separation. However, S also checkerboarded, so none of the simulated models were able to replicate the distal features of S (features *ii* and *iii*). While we observed a subset of models with on-diagonal enrichment of S_{intra} contacts (feature *i*), it was always accompanied by off-diagonal enrichment of S-S_{inter} contacts—contrary to the depletion required for feature *ii*.

To further understand this relationship, we quantified contact enrichment and depletion from $^{observed}/_{expected}$ (Materials and Methods) Hi-C maps for each model. We assessed whether the Hi-C maps were consistent with the first two S features (S_{intra} and S-S_{inter}) using the most lenient criteria: enrichment was defined as an average $^{observed}/_{expected}$ pixel strength greater than one, while depletion was defined as $^{observed}/_{expected}$ less than one. This analysis confirmed that none of the phase separation models accurately captured the experimentally observed features of S. Enrichment of S_{intra} (feature *i*) and depletion of S-S_{inter} (feature *ii*) did not co-occur because contact enrichment within contiguous domains (S_{intra}, feature *i*) was correlated with contact enrichment between S domains (S-S_{inter}, opposite of feature *ii*). By quantifying compartment strength from each Hi-C map (color scale in Figure 3C, right), we found that both S_{intra} and S-S_{inter} enrichment increased as chromatin compartmentalization strengthened. As evident in the simulated Hi-C maps, models with sufficiently high A-to-A and

B-to-B affinities to produce A/B checkerboarding always resulted in S-S_{inter} enrichment and S checkerboarding (Figure 3C, Figure S5A). Together with polymer conformations and the Hi-C maps (Figure 3C, left), these results indicate that phase separation of A and B chromatin induces phase separation of S chromatin, even in the absence of S self-attraction.

To confirm that phase separation of S leads to these undesired, conventional compartment patterns in S (enriched S-S_{inter} and S checkerboarding), we introduced self-attraction to S monomers and repeated the A-to-A and B-to-B affinity sweep. As expected, S-to-S self-attraction resulted in increased S_{intra}, S-S_{inter}, and S checkerboarding (Figure S5B). We therefore conclude that phase separation does not drive S-like organization.

Uniform loop extrusion with A and B phase separation

Informed by evidence of loop extrusion activity in the PD-D2 Hi-C maps (Figure 2J and 2K), we tested whether loop extrusion plays a role in S compartment formation. Given that TAD formation via the loop extrusion process results in domain enrichment and compartment suppression [27,32,49,50], we hypothesized that loop extrusion might promote S_{intra} contacts (feature *i*, domain enrichment) while suppressing both S-S_{inter} contacts and the checkering of S (features *ii* and *iii*, compartment suppression). We therefore tested whether S domains are akin to TADs in vertebrates, formed by uniformly loaded, genome-wide loop extruders that are stalled by barriers.

In these models, loop extruders randomly bind to the chromatin fiber and progressively extrude the chromatin polymer into loops. Extrusion proceeds until the extruder unbinds or stalls. Given the evidence for extrusion barriers in and at the edges of S domains (Figure 2K), we placed loop-extrusion-stalling sites at the ends of S domains. We then varied the relevant simulation parameters: A and B homotypic affinities, mean separations between extruders (d), and extruder processivity (λ, the average loop size extruded by an unobstructed extruder). We assumed S monomers lacked preferential attractions to other S monomers.

As evident in the resulting contact maps, these models cannot generate S compartments (Figure 3D, left). We observed on-diagonal extrusion domains in S, with barrier features visually similar to those in the experimental Hi-C data (feature *i*). However, we did not observe off-diagonal depletion of contacts (feature *ii*). Like the phase-separation-only models, this class of models failed to achieve the desired compartment-level organization. Though loop extrusion counteracted compartmentalization, this antagonistic effect was not restricted to S; when compartment features (checkering off-diagonal contacts) were suppressed in S, they were likewise suppressed in A and B. Conversely, when compartment checkerboarding was present in A and B, it was also present in S.

Similar to the phase-separation-only models, upon quantifying Hi-C contact enrichments, we found that S_{intra} and S-S_{inter} contacts are highly correlated and are largely reflective of compartment strength (Figure 3D, right). Consistent with the antagonism between loop extrusion and compartmentalization, stronger extrusion (smaller separations and/or larger processivities) demands higher affinities to achieve the same level of compartmentalization (Figure S5C). While two models narrowly satisfied the quantitative criteria for features *i* and *ii*, we find that their Hi-C maps visually lacked compartmentalization of any type (S-S_{inter} ≈ A-A ≈ B-B contacts, all low), as expected for the high density of extruders (d = 50 kb) (Figure 3D, left). We conclude that the uniform loading model is unable to reliably

generate S compartments. Therefore, the presence of S features strongly indicates that some aspect of the loop extrusion process in *B. mori* differs from that of vertebrates.

Loop extrusion with targeted loading in S and A/B phase separation

To preferentially suppress compartmentalization of S (off diagonal S features - *ii* and *iii*) while preserving them in A and B, we hypothesized that loop extrusion may be targeted to S. We therefore tested a new class of models in which loop extruders were more likely to load in S than in A and B, resulting in lower mean separation of extruders in S (d_S) than in A and B ($d_{A\&B}$). Our hypothesis of more extruders in S would lead to smaller loops in S, consistent with our observations from the Hi-C data (Figure 2J).

Models with targeted loading to S reliably produced S-like features in their Hi-C maps, unlike the previous two classes of models. Weak extrusion in A and B allowed A/B compartments to form, while strong extrusion in S both compacted S domains (S_{intra} enriched, feature *i*) and inhibited S-S_{inter} compartment contacts (feature *ii*) (Figure 3E, left). Additionally, Hi-C maps with weaker extrusion in A and B had smoother lanes of S depletion (feature *iii*).

Analyzing the Hi-C maps quantitatively showed that targeting loading of extruders to S alters the balance between S_{intra} and S-S_{inter} contacts (Figure 3E, right). As extrusion in A and B weakened ($d_{A\&B}$ increased, increased relative targeting), both features *i* and *ii* began to look more S-like: S_{intra} enrichment strengthened (gain of feature *i*) and distal S-S_{inter} enrichment was lost (gain of feature *ii*). Therefore, unlike the phase-separation-only and uniform loop extrusion models, targeting extrusion to S domains both compacts S and secludes them from contacting each other.

Additionally, models with stronger targeted loading produced S features more robustly. First, decreasing extrusion in A and B (increasing $d_{A\&B}$) allowed features *i* and *ii* to co-exist across a broader range of compartment strengths (Figure 3F). Furthermore, S features persist upon the introduction of S-to-S affinity comparable to those of A-to-A and B-to-B (Figure S5D).

We next measured feature *iii* as the standard deviation of average $^{observed}/_{expected}$ S-A, S-B, and S-S_{inter} contact frequencies. Smoother lanes of depletion (off-diagonal S contacts) result in smaller standard deviations. In the uniform loading model, once compartment features began to emerge (compartment strength > 0.1), the standard deviation increased (feature *iii* disappeared), indicating a less smooth pattern of inter-compartmental contacts. However, as extrusion in A and B decreased (more targeted loading, i.e. $d_{A\&B}$ increased), higher compartment scores could be tolerated before S smoothness was lost. We found that the gain in smoothness (small standard deviation) due to targeted loading is largely driven by the suppression of S-S_{inter} (feature *ii*) as well as additional contributions from A/B compartmentalization (Figure S5E).

Thus, preferential loading of loop extruders to S in combination with self-affinities of A and B reliably produces the patterns of *B. mori* Hi-C maps. The latter compartmentalize the genome, while loop extrusion targeted to S generates the unique features of S compartments.

The different features of S rely on distinct aspects of targeted extrusion and compartmentalization

To understand how these principles generate the specific folding patterns of *B. mori* chromosomes, we developed a quantitative chromosome-scale model employing the principles from the minimal model study. Focusing on a 6.5 Mb segment of chromosome 15

411 (Figure 4A), we assigned compartment identities to the simulated chromosome based on
412 those from the PD-D2 Hi-C maps. To compare models to experimental Hi-C, we computed
413 $^{observed}/_{expected}$ contact enrichments between all types of compartments, partitioning S-S
414 contacts into S-S_{inter} and S_{intra}. Models varied in five parameters: A-to-A affinity, B-to-B affinity,
415 extruder processivity (λ), the average separation between extruders inside S (d_S), and the
416 average separation between extruders outside of S (inside A and B regions, $d_{A\&B}$).
417 We first reaffirmed our key findings from the minimal model that neither phase
418 separation alone (Figure 4B) nor with uniform extrusion (TAD-like) (Figure 4C) can generate
419 secluded S domains. For phase separation-only models, we varied A and B homotypic affinities
420 in the absence of loop extrusion, but this did not produce the desired combination of S_{intra}
421 (feature *i*) and S-S_{inter} values (feature *ii*) (Figure 4C). With uniform extrusion, we similarly could
422 not reproduce features *i* and *ii* quantitatively, regardless of processivity (λ) or extruder density
423 (d_S) (Figure 4C). For the targeted loading models, some, but not all, models quantitatively
424 reproduced experimental values for features *i* and *ii*. We noticed that different aspects of
425 extrusion dynamics influenced either feature *i* or feature *ii* (Figure 4D). Specifically, the *relative*
426 abundance of extruders in S versus A and B ($d_{A\&B}/d_S$) appeared to have a strong effect on
427 feature *i*. Likewise, the overall abundance of extruders in S (separation in S, d_S) influenced
428 feature *ii* (Figure 4D, arrows). These observations prompted us to more deeply investigate
429 how different parameters of our model control the different features of S.
430 We first asked how such strong domains of S_{intra} contacts (feature *i*) arise from targeted
431 loading. We systematically varied processivity (λ), mean extruder separation in S (d_S), and
432 mean separation in A and B ($d_{A\&B}$) independently. Consistent with Figure 4D, our simulations
433 revealed that feature *i* is driven by the *relative* abundance of loop extruders in S ($d_{A\&B}/d_S$) and
434 is insensitive to processivity (Figure 4E). For a given set of compartment affinities (A-to-A
435 affinity = 0.12 kT, B-to-B affinity = 0.04 kT), achieving the desired level of relative compaction
436 (S_{intra} = 1.78, feature *i*) required extruders to be approximately ten-fold more abundant in S
437 compared to A and B (i.e., $d_{A\&B}/d_S \approx$ 10-15, Figure 4E). Increasing A/B compartment strength
438 allowed relative abundance in S to decrease slightly to achieve the desired S_{intra} enrichment
439 ($d_{A\&B}/d_S \approx$ 5-10, Figure S6A). This suggests that S compaction results from substantial
440 recruitment of extruders to S, comparable to targeted cohesin loading in other contexts [43].
441 We next uncovered that S-to-S compartment attenuation (feature *ii*) is predominantly
442 controlled by the overall abundance of extruders in S (d_S) (Figure 4F). This contrasts with
443 vertebrates, where extrusion modulates compartment strength by both extruder processivity
444 (λ) and separation (d). Because S domains are small (median 75 kb for our simulated region),
445 even modest extruder processivities ($\geq$ 56 kb) generate high loop coverage in S (Figure S6B).
446 Therefore, extruder abundance governs S compaction (Figure S6C) and in turn S-S_{inter} seclusion
447 (Figure 4F). To generate distal S-S_{inter} depletions similar to those measured in the Hi-C, the
448 abundance of extruders in S must be high (small d_S). Based on the modeled region, where the
449 experimentally measured $^{observed}/_{expected}$ S-S_{inter} depletion (feature *ii*) is 0.7, we estimate
450 extruder separation (d_S) is 20-40 kb (Figure 4F). A precise estimate depends on the strength
451 of A/B compartmentalization, as stronger compartmentalization can promote S-S_{inter} contacts
452 (i.e., loss of feature *ii*, Figure S6D).
453 We next sought to explain the most notable feature in *B. mori* Hi-C maps: S smoothness
454 (feature *iii*). For smooth lanes of contact depletion, S must be similarly depleted in contacts

455 with A, B, and other S domains. While S-S_{inter} depletion (Figure 4F) is primarily controlled by
456 extrusion in S (d_S), loop extrusion in S has only a minor effect on S-A and S-B contacts (Figure
457 S6E). Rather, S-A and S-B contacts are predominantly controlled by A and B phase separation:
458 loss of S-A and S-B contacts reflect the demixing (phase separation) of A and B, respectively
459 (Figure S6E). Therefore, to achieve similar levels of S-A and S-B contacts, the level of phase
460 separation of A and B must be approximately equal (i.e. $^{observed}/_{expected}$ A-A contacts ≈
461 $^{observed}/_{expected}$ B-B contacts). Additionally, when A/B compartmentalization strengthens,
462 smoothness is also lost because S-S_{inter} increases. Therefore, A/B compartmentalization must
463 be low to maintain smoothness (Figure 4G, Figure S6E and S6F).
464 We find *B. mori* chromatin organization arises from a unique interplay of multiple
465 parameters, allowing us to estimate model parameters (d_S, $d_{A\&B}/d_S$, A-to-A, and B-to-B
466 affinities) from the different Hi-C features of S (Figures 4E-G). To develop a quantitatively
467 accurate *B. mori* chromosomal model, we integrated our estimates and insights from Figures
468 4E-G, sweeping over estimated extrusion and compartment parameters. Models with high
469 levels of targeted extrusion (such as d_S = 19 kb, $d_{A\&B}$ = 190 kb; $d_{A\&B}/d_S$ = 10) and equally modest
470 A and B compartmentalization reproduced Hi-C maps qualitatively and $^{observed}/_{expected}$
471 enrichments quantitatively (Figures 4H, 4I). Other successful models also had these
472 characteristics (Figure 4I). As predicted, models with any parameter outside of estimated
473 ranges (increasing d_S, reducing $d_{A\&B}$, high or unequal A-A and B-B contact strength)
474 systematically caused models to fail.
475 Our models reveal a previously uncharacterized interplay of loop extrusion and
476 chromatin compartmentalization in shaping the genome. Loop extrusion in *B. mori* is targeted
477 to S domains, which leads to higher S compaction and suppression of (off-diagonal)
478 compartment contacts between S. Together, these mechanisms generate the striking
479 chromatin contact patterns that dictate 3D genome architecture. We next used our *B. mori*
480 chromosomal model to make predictions on spatial localization.
481
482 *S domains are preferentially found on the surfaces of chromosome territories*

483 The spatial partitioning of active and inactive chromatin within the nucleus has
484 previously been attributed to conventional compartmentalization [33]. We asked whether the
485 seclusion of compartment S confers distinct spatial positioning using our best-performing
486 model of chromosome 15 (Figure 4H). By analyzing the radial positioning of A, B, and S, we
487 found a strong preference for S domains to localize to the periphery of chromosome territories
488 (CTs) (Figures 5A, 5B). A and B both showed preference for localizing to the center of the
489 territory, with A being more centrally biased. When compared to an analogous model without
490 extrusion, S was more interspersed throughout the territory. Models with higher targeting of
491 extrusion to S (no loading in A and B) showed even stronger radial preference of S. Therefore,
492 our models predict that extrusion in S modulates its spatial localization, biasing it to the
493 periphery of CTs.
494 To test these findings, we used Oligopaint FISH to label portions of single A, B, or S
495 domains as well as the whole CTs for Chr04, Chr17, and Chr23 in embryonic nuclei (Figures 5C,
496 S7B and S7C). Shell analysis (Material and Methods) revealed that S domains are more likely
497 to occupy peripheral CT shells compared to A and B domains (Figure 5D). In addition,
498 measuring the distance from the domain center to the CT edge showed that S domains are

499 closer to the CT edge than A or B domains for all chromosomes and loci analyzed (Figure S7D).
500 These observations were confirmed by additional experiments with super-resolution
501 microscopy (Figure S7E and S7F).
502 Although inter-chromosomal contacts were sparse in the Hi-C data, we asked whether
503 this peripheral localization could influence the average contact frequency among S domains
504 in *trans*. Therefore, we computed the average *trans* $^{observed}/_{expected}$ contacts between each
505 compartment type (Figure 5E). We found that the average value of S-S_{inter} *trans* contacts is
506 higher compared to any other combination in *trans*, and, in particular, A-A and B-B contacts.
507 This is consistent with the preferential positioning of S towards the periphery of CTs, a favored
508 location for *trans* contacts.
509 Our DNA FISH reveal S domains are preferentially located at the CT peripheries, which
510 is further supported by the Hi-C. Our modeling indicates that this may be caused by a
511 previously unknown effect of loop extrusion: its ability to influence the spatial positioning of
512 chromatin in the context of its chromosome territory.
513
514 *Compartment S changes during development*

515 Taking advantage of our Hi-C datasets from different developmental stages, including
516 three embryonic stages and one adult stage, we next explored the developmental dynamics
517 of compartment S. Based on initial visual inspections, we could identify domains switching to
518 or from S on multiple chromosomes between timepoints (see examples in Figure S8A). To test
519 the dynamics of S compartment switching more systematically, we repeated the
520 compartment calling protocol for the adult stage (Adult Heads, AH). We found that a
521 comparable fraction of the AH genome (12%) folds into compartment S, compared to the PD-
522 D2 embryonic stage (Figure S8B). Nevertheless, several embryonic S domains visually show
523 checkerboard patterning in the AH Hi-C maps, including three of the largest S domains on
524 Chr06 and Chr23 (Figures 6A and S8C). To compare the two datasets further, we restricted our
525 analyses to large (>200 kb) domains to allow for visual confirmation of compartment
526 assignment based on the Hi-C contact pattern. We found that about 45% of S domains defined
527 in the PD-D2 embryonic stage are maintained in the AH (referred to as S->S) (Figure 6B). This
528 fraction is much lower compared to that of the A or B domains. Large S domains that change
529 compartment assignment in the AH exclusively turn into B domains (referred to as S->B).
530 Notably, this change coincides with a significant reduction in gene expression levels (Figures
531 6C and S8D). The Hi-C contact maps at S domains that turn into B show a loss of features
532 associated with loop extrusion, including insulation points and off-diagonal dots (Figures 6A
533 and S8C). Weakening of insulation is also evident when comparing pileup contact enrichments
534 of boundaries called within large S domains that are maintained (S->S) or lost (S->B) in the AH
535 data (Figure 6D). The loss of extrusion features and intra-domain compaction, together with
536 the increased checkerboard patterning of S domains that turn into B, are consistent with our
537 model that targeted loop extrusion underlies the spatial segregation of compartment S by
538 counteracting compartmentalization.
539 To test whether the change in compartment identity also translate to a change in
540 domain position within CTs, we took advantage of the fact that one of the three S domains
541 that we chose for Oligopaint FISH analyses turned into B in the AH Hi-C dataset. Consistent
542 with the change in compartment identity, super-resolution microscopy revealed that the

543 same region on Chr04 localizes more internally in its CT in nuclei of the adult *B. mori* head
544 compared to embryos (Figure 6E and F). In contrast, a B domain used as a control remained
545 unchanged between the two stages (Figure S8E and F). These results were further validated
546 using wide-field microscopy, labeling A, B, and S domains as well as the entire CT on Chr04 in
547 AH. Notably, in AH cells, the S domain that transitioned into B no longer exhibited a tendency
548 to be positioned closer to the CT periphery (Figure S8G and H). The developmental dynamics
549 of several S domains argue against a strict genetic specification of compartment S but rather
550 support the presence of epigenetic features involved in its formation.
551
552 **Discussion**

553 Our investigation of *B. mori*'s genome organization reveals both conserved principles
554 and novel genome-folding behaviors. As seen in other eukaryotes, we observe the formation
555 of CTs and spatial segregation of chromatin into active A and inactive B compartments.
556 However, unlike other eukaryotes, we have observed much stronger chromosome
557 territoriality and a novel type of compartment, S, which lacks the characteristic
558 checkerboarding of A/B compartments and appears to be rich in loop extrusion activity. Our
559 modeling indicates that a unique interplay of chromatin compartmentalization and loop
560 extrusion may drive the formation of these spatially secluded domains that appear to change
561 throughout development.
562 The remarkably strong CTs and the low frequency of inter-chromosomal contacts are
563 consistent with a recent whole-chromosome Oligopaint study of six *B. mori* chromosomes,
564 which likewise revealed highly spatially distinct CTs [73]. Folding, volume, and intermixing of CTs
565 have been associated with condensin II [64,94]. Condensin II subunits are present in the *B. mori*
566 genome [95,96] and it would be interesting to evaluate whether the substantial degree of
567 territoriality is caused by uniquely high activity of condensin II in *B. mori*. CT strength is also
568 intriguing from an evolutionary point of view. Previous studies in *D. melanogaster* cell lines [97]
569 and across human cancers [98] have described an inverse relationship between the frequency
570 of inter-chromosomal contacts and the incidence of genomic translocations. Interestingly,
571 karyotypes and synteny are highly conserved across Lepidoptera, including *B. mori*. We
572 therefore hypothesize that the pronounced CTs may contribute to low structural variation and
573 high karyotype conservation in these organisms by preventing structural rearrangements
574 during mitotic divisions of cells destined to form the future germline.
575 The presence of compartment S, with domains that strongly self-interact but segregate
576 from the rest of their chromosome, is remarkable. To our knowledge, there is no precedent
577 for a compartment with contact or epigenetic profiles similar to compartment S. While other
578 compartment types beyond A and B have been detected [40,82,99], they typically represent sub-
579 types of A and B and show preferential homotypic contacts [82]. Although the previously
580 described "intermediate" compartment I [27,100,101] shares some characteristics with
581 compartment S, such as H3K27me3 enrichment and developmental plasticity, they differ in
582 their most prominent features. Compartment I is *enriched* in contacts with A, B, and I. A
583 recently identified sub-compartment in HCT116 cells, termed B_0 [82], likewise displays relatively
584 low levels of compartment contrast (i.e., its compartments are smoother and they
585 checkerboard less than other compartment types), though it does preferentially interact with

586 other B_0 domains. Domains of compartment S, in contrast to I or B_0, are homogenously
587 *depleted* in contacts with any other domain. This pattern, plus their gene composition and
588 distinct epigenetic makeup, make S unique compared to any previously identified chromatin
589 structure.

590 The formation of compartment S appears to require an interplay of mechanisms,
591 distinct from any other described organism. While conventional compartmentalization is
592 believed to rely on affinity between regions that share epigenetic composition [102], we show
593 that affinity-mediated phase separation cannot lead to the formation of compartment S.
594 Instead, we propose that compartment S is formed by loop extrusion activity targeted to S
595 domains. Targeting extrusion to S domains selectively compacts them and suppresses their
596 compartmentalization. This loop extrusion behavior is different than in vertebrates, where
597 loop extruding cohesin (during interphase) and condensin (in metaphase) are believed to load
598 mostly uniformly across the genome, without preference for a specific compartment type [28,82].
599 Such localization of extruders to many broad epigenetic domains (tens to hundreds of kb each)
600 has not been identified in other systems.

601 Targeted SMC loading to certain genetic elements is well-described across various
602 biological systems. In the bacterium *B. subtilis*, condensins are loaded at *ParS* sites by the ParB
603 DNA-binding protein [103,104]. In yeast, it has been suggested that sequence context antagonizes
604 SMCs from centromere binding [105]. In *C. elegans*, direct loading of condensin^{DC} to specific
605 sequences (rex sites) direct the SMC-containing dosage compensation complex to the sex
606 chromosome [65,106]. Most recently, targeted loading of SMCs to enhancers has been shown to
607 form fountains or jets in Hi-C maps in *C. elegans* [44,47] and vertebrates [42,43,107]. Such targeted
608 loading in these systems may be guided by differences in DNA accessibility, sequence-specific
609 DNA binding proteins [103,104], or via enhancer-specific histone marks [42,43,107]. We speculate that
610 such factors may target loop-extruding complexes to compartment S in *B. mori*.

611 In the context of targeted loading of SMC complexes, the enrichment of H4K20me1 in
612 compartment S is interesting. In *C. elegans*, it has been shown that the SMC-based dosage
613 compensation complex enriches H4K20me1 on the inactive sex chromosome by means of a
614 condensin-associated demethylase [86]. H4K20me1 is likewise deposited during the process of
615 silencing and compacting the X chromosome in mice [108]. Compartment S shares similarity to
616 inactivated sex chromosomes by virtue of being locally compacted and isolated from the rest
617 of the genome, while it is distinct from inactivated sex chromosomes by virtue of its
618 permissiveness to gene expression. Whether enrichment of H4K20me1 aids in chromatin
619 compaction, and what its relationship is to loop extrusion, is unclear for *B. mori*.

620 In addition, our analyses also support a previously unknown consequence of loop
621 extrusion. Not only does loop extrusion activity lead to the formation of dense and secluded
622 S domains, but it also drives their peripheral localization within CTs. This effect of loop
623 extrusion is a novel finding, raising the possibility that loop extrusion may similarly affect large-
624 scale spatial organization in other organisms or contexts. The underlying physics by which
625 extrusion can achieve this architecture is yet to be understood.

626 The function of compartment S and the role of loop extrusion there remain intriguing
627 questions. First, in view of the holocentric architecture of *B. mori* chromosomes, we consider
628 the possibility that compartment S is involved in centromere specification to be unlikely. This
629 conclusion is guided by our previous findings in *B. mori* cell lines showing that kinetochore
630 assembly occurs in regions anticorrelated with transcriptionally active chromatin [109] - an
631 epigenetic landscape that is more consistent with compartment B than S. Instead, the isolated
632 genomic environment of S domains might ensure the precise transcriptional regulation of the

633 genes that they contain. Our finding that S-located genes are functionally enriched in
634 transcription-related processes might suggest that S represents a developmental transition
635 state to either A or B, as hypothesized for compartments I and B_0 [82,100,101]. Such a model is
636 supported by the observation that many S domains are variable among different
637 developmental stages. Furthermore, S domains may represent development-control units,
638 such as the Hox cluster, which comprises a large S domain in *B. mori* embryos (Figure S4). By
639 analogy to the Hox cluster, where loop extrusion appears to be key to the precise sequence
640 of gene activation [110], compartment S may recruit a high density of extruders to achieve
641 precisely timed activation of genes during development. Our observation of developmental
642 plasticity of S domains supports this hypothesis.
643 In summary, our study describes the unique genome organization of *B. mori.* This non-
644 model organism has an exceptional degree of chromosome territoriality and reveals a striking
645 new genome folding structure. Our modeling indicates that this novel structure, compartment
646 S, can be formed by loop extrusion targeted to a specific chromatin type. Genome
647 organization in *B. mori* thus demonstrates that the interplay of two major genome-folding
648 processes, loop extrusion and compartmentalization, can generate unique and unexpected
649 patterns. These findings open a new line of questions for how evolutionarily conserved
650 mechanisms may interact differently in different organisms, as well as how changes in the
651 epigenetic landscape during development can guide loop extrusion to reshape 3D genome
652 architecture.
653
654

Acknowledgements:
We would like to thank the members of the Lei, Mirny, and Drinnenberg labs, as well as Job Dekker and Axel Cournac for their helpful discussions. We thank Max Imakaev for extensive, critical feedback on the manuscript. We thank all members of the Koszul lab and in particular Pierrick Moreau for helping in the initial development of the Hi-C protocol. We thank Stéphane Descorps-Declère, Ilya M. Flyamer, and Nicolas Servant for their help in using bioinformatics tools. We would also like to thank Life Science Editors for editing services (www.lifescienceeditors.com). EN is funded by the National Science Foundation's Graduate Research Fellowship. This work of LAM is supported by NIH GM114190 and NSF-ANR Program (ANR-22-CE95-0003). LAM is also a recipient of the « Chaires Internationales de Recherche Blaise Pascal » and the CNRS Fellow-Ambassador award. HM and IAD receive salary support from the CNRS. This work is supported by the Labex DEEP ANR-11-LABX-0044 part of the IDEX Idex PSL ANR-10-IDEX-0001-02 PSL, an ATIP-AVENIR Research grant, the FRM and Fondation Schlumberger (FSER202202015420), Institut Curie, the ERC (CENEVO-758757), and INSB «Diversity of biological mechanisms». This work was supported in part by the Intramural Program of the National Institute of Diabetes and Digestive and Kidney Diseases, National Institutes of Health (NIDDK; DK015602 to E.P.L.), the Eunice Kennedy Shriver National Institute of Child Health, and Human Development, National Institutes of Health (NICHD; 1K99HD104851 to L.F.R).

674 REFERENCES:

675 1. Seitan, V. C. *et al.* Cohesin-based chromatin interactions enable regulated gene expression
676 within preexisting architectural compartments. *Genome Res.* **23**, 2066–2077 (2013).
677 2. Hnisz, D. *et al.* Activation of proto-oncogenes by disruption of chromosome
678 neighborhoods. *Science* **351**, 1454–1458 (2016).
679 3. Lupiáñez, D. G. *et al.* Disruptions of topological chromatin domains cause pathogenic
680 rewiring of gene-enhancer interactions. *Cell* **161**, 1012–1025 (2015).
681 4. Brückner, D. B., Chen, H., Barinov, L., Zoller, B. & Gregor, T. Stochastic motion and
682 transcriptional dynamics of pairs of distal DNA loci on a compacted chromosome. *Science*
683 **380**, 1357–1362 (2023).
684 5. Ogiyama, Y., Schuettengruber, B., Papadopoulos, G. L., Chang, J.-M. & Cavalli, G.
685 Polycomb-Dependent Chromatin Looping Contributes to Gene Silencing during Drosophila
686 Development. *Mol Cell* **71**, 73-88.e5 (2018).
687 6. Kiefer, L. *et al.* WAPL functions as a rheostat of Protocadherin isoform diversity that
688 controls neural wiring. *Science* **380**, eadf8440 (2023).
689 7. Kiefer, L. *et al.* Tuning cohesin trajectories enables differential readout of the Pcdhα
690 cluster across neurons. *Science* **385**, eadm9802 (2024).
691 8. Misteli, T. The Self-Organizing Genome: Principles of Genome Architecture and Function.
692 *Cell* **183**, 28–45 (2020).
693 9. Jackson, D. A. & Pombo, A. Replicon clusters are stable units of chromosome structure:
694 evidence that nuclear organization contributes to the efficient activation and propagation
695 of S phase in human cells. *J Cell Biol* **140**, 1285–1295 (1998).
696 10. Nakatani, T. *et al.* Emergence of replication timing during early mammalian development.
697 *Nature* **625**, 401–409 (2024).
698 11. Piazza, A. *et al.* Cohesin regulates homology search during recombinational DNA repair.
699 *Nat Cell Biol* **23**, 1176–1186 (2021).
700 12. Arnould, C. *et al.* Loop extrusion as a mechanism for formation of DNA damage repair foci.
701 *Nature* **590**, 660–665 (2021).
702 13. Dekker, J. & Mirny, L. A. The chromosome folding problem and how cells solve it. *Cell* **187**,
703 6424–6450 (2024).
704 14. Peters, J.-M. How DNA loop extrusion mediated by cohesin enables V(D)J recombination.
705 *Curr Opin Cell Biol* **70**, 75–83 (2021).
706 15. Batty, P. & Gerlich, D. W. Mitotic Chromosome Mechanics: How Cells Segregate Their
707 Genome. *Trends Cell Biol* **29**, 717–726 (2019).
708 16. Ghosh, R. P. & Meyer, B. J. Spatial Organization of Chromatin: Emergence of Chromatin
709 Structure During Development. *Annu Rev Cell Dev Biol* **37**, 199–232 (2021).
710 17. Lichter, P., Cremer, T., Borden, J., Manuelidis, L. & Ward, D. C. Delineation of individual
711 human chromosomes in metaphase and interphase cells by in situ suppression
712 hybridization using recombinant DNA libraries. *Hum Genet* **80**, 224–234 (1988).
713 18. Cremer, T. & Cremer, C. Chromosome territories, nuclear architecture and gene regulation
714 in mammalian cells. *Nat Rev Genet* **2**, 292–301 (2001).
715 19. Hildebrand, E. M. *et al.* Mitotic chromosomes are self-entangled and disentangle through
716 a topoisomerase-II-dependent two-stage exit from mitosis. *Mol Cell* **84**, 1422-1441.e14
717 (2024).
718 20. Lieberman-Aiden, E. *et al.* Comprehensive mapping of long-range interactions reveals
719 folding principles of the human genome. *Science* **326**, 289–293 (2009).

720 21. Wang, S. *et al.* Spatial organization of chromatin domains and compartments in single
721 chromosomes. *Science* **353**, 598–602 (2016).
722 22. Banigan, E. J. & Mirny, L. A. Loop extrusion: theory meets single-molecule experiments.
723 *Curr Opin Cell Biol* **64**, 124–138 (2020).
724 23. Yatskevich, S., Rhodes, J. & Nasmyth, K. Organization of Chromosomal DNA by SMC
725 Complexes. *Annu Rev Genet* **53**, 445–482 (2019).
726 24. Fudenberg, G. *et al.* Formation of Chromosomal Domains by Loop Extrusion. *Cell Rep* **15**,
727 2038–2049 (2016).
728 25. Sanborn, A. L. *et al.* Chromatin extrusion explains key features of loop and domain
729 formation in wild-type and engineered genomes. *Proc Natl Acad Sci U S A* **112**, E6456-6465
730 (2015).
731 26. Rao, S. S. P. *et al.* Cohesin Loss Eliminates All Loop Domains. *Cell* **171**, 305-320.e24 (2017).
732 27. Schwarzer, W. *et al.* Two independent modes of chromatin organization revealed by
733 cohesin removal. *Nature* **551**, 51–56 (2017).
734 28. Gibcus, J. H. *et al.* A pathway for mitotic chromosome formation. *Science* **359**, (2018).
735 29. Goloborodko, A., Marko, J. F. & Mirny, L. A. Chromosome Compaction by Active Loop
736 Extrusion. *Biophys J* **110**, 2162–2168 (2016).
737 30. Mirny, L. A., Imakaev, M. & Abdennur, N. Two major mechanisms of chromosome
738 organization. *Curr Opin Cell Biol* **58**, 142–152 (2019).
739 31. Jost, D., Carrivain, P., Cavalli, G. & Vaillant, C. Modeling epigenome folding: formation and
740 dynamics of topologically associated chromatin domains. *Nucleic Acids Res* **42**, 9553–9561
741 (2014).
742 32. Nuebler, J., Fudenberg, G., Imakaev, M., Abdennur, N. & Mirny, L. A. Chromatin
743 organization by an interplay of loop extrusion and compartmental segregation. *Proc. Natl.*
744 *Acad. Sci. U.S.A.* **115**, E6697–E6706 (2018).
745 33. Falk, M. *et al.* Heterochromatin drives compartmentalization of inverted and conventional
746 nuclei. *Nature* **570**, 395–399 (2019).
747 34. Murphy, S. E. & Boettiger, A. N. Polycomb repression of Hox genes involves spatial
748 feedback but not domain compaction or phase transition. *Nat Genet* **56**, 493–504 (2024).
749 35. Owen, J. A., Osmanović, D. & Mirny, L. Design principles of 3D epigenetic memory systems.
750 *Science* **382**, eadg3053 (2023).
751 36. Kraft, K. *et al.* Polycomb-mediated genome architecture enables long-range spreading of
752 H3K27 methylation. *Proc Natl Acad Sci U S A* **119**, e2201883119 (2022).
753 37. Nora, E. P. *et al.* Spatial partitioning of the regulatory landscape of the X-inactivation
754 centre. *Nature* **485**, 381–385 (2012).
755 38. Sexton, T. *et al.* Three-dimensional folding and functional organization principles of the
756 Drosophila genome. *Cell* **148**, 458–472 (2012).
757 39. Dixon, J. R. *et al.* Topological domains in mammalian genomes identified by analysis of
758 chromatin interactions. *Nature* **485**, 376–380 (2012).
759 40. Rao, S. S. P. *et al.* A 3D map of the human genome at kilobase resolution reveals principles
760 of chromatin looping. *Cell* **159**, 1665–1680 (2014).
761 41. Vian, L. *et al.* The Energetics and Physiological Impact of Cohesin Extrusion. *Cell* **173**, 1165-
762 1178.e20 (2018).
763 42. Guo, Y. *et al.* Chromatin jets define the properties of cohesin-driven in vivo loop extrusion.
764 *Mol Cell* **82**, 3769-3780.e5 (2022).

43. Galitsyna, A. *et al.* Extrusion fountains are hallmarks of chromosome organization emerging upon zygotic genome activation. *bioRxiv* 2023.07.15.549120 (2023) doi:10.1101/2023.07.15.549120.
44. Kim, J., Wang, H. & Ercan, S. Cohesin organizes 3D DNA contacts surrounding active enhancers in C. elegans. *Genome Res* **35**, 1108–1123 (2025).
45. Shao, W. *et al.* The jet-like chromatin structure defines active secondary metabolism in fungi. *Nucleic Acids Res* **52**, 4906–4921 (2024).
46. Wike, C. L. *et al.* Chromatin architecture transitions from zebrafish sperm through early embryogenesis. *Genome Res* **31**, 981–994 (2021).
47. Isiaka, B. N. *et al.* Cohesin forms fountains at active enhancers in C. elegans. *bioRxiv* 2023.07.14.549011 (2023) doi:10.1101/2023.07.14.549011.
48. Gassler, J. *et al.* A mechanism of cohesin-dependent loop extrusion organizes zygotic genome architecture. *EMBO J.* **36**, 3600–3618 (2017).
49. Wutz, G. *et al.* Topologically associating domains and chromatin loops depend on cohesin and are regulated by CTCF, WAPL, and PDS5 proteins. *EMBO J.* **36**, 3573–3599 (2017).
50. Haarhuis, J. H. I. *et al.* The Cohesin Release Factor WAPL Restricts Chromatin Loop Extension. *Cell* **169**, 693-707.e14 (2017).
51. Goel, V. Y. *et al.* Dynamics of microcompartment formation at the mitosis-to-G1 transition. *bioRxiv* 2024.09.16.611917 (2024) doi:10.1101/2024.09.16.611917.
52. Lengronne, A. *et al.* Cohesin relocation from sites of chromosomal loading to places of convergent transcription. *Nature* **430**, 573–578 (2004).
53. Gullerova, M. & Proudfoot, N. J. Cohesin complex promotes transcriptional termination between convergent genes in S. pombe. *Cell* **132**, 983–995 (2008).
54. Glynn, E. F. *et al.* Genome-wide mapping of the cohesin complex in the yeast Saccharomyces cerevisiae. *PLoS Biol.* **2**, E259 (2004).
55. Bausch, C. *et al.* Transcription alters chromosomal locations of cohesin in Saccharomyces cerevisiae. *Mol Cell Biol* **27**, 8522–8532 (2007).
56. Tran, N. T., Laub, M. T. & Le, T. B. K. SMC Progressively Aligns Chromosomal Arms in Caulobacter crescentus but Is Antagonized by Convergent Transcription. *Cell Rep* **20**, 2057–2071 (2017).
57. Brandão, H. B. *et al.* RNA polymerases as moving barriers to condensin loop extrusion. *Proc Natl Acad Sci U S A* **116**, 20489–20499 (2019).
58. Busslinger, G. A. *et al.* Cohesin is positioned in mammalian genomes by transcription, CTCF and Wapl. *Nature* **544**, 503–507 (2017).
59. Banigan, E. J. *et al.* Transcription shapes 3D chromatin organization by interacting with loop extrusion. *Proc Natl Acad Sci U S A* **120**, e2210480120 (2023).
60. Le, T. B. K., Imakaev, M. V., Mirny, L. A. & Laub, M. T. High-resolution mapping of the spatial organization of a bacterial chromosome. *Science* **342**, 731–734 (2013).
61. Marbouty, M. *et al.* Condensin- and Replication-Mediated Bacterial Chromosome Folding and Origin Condensation Revealed by Hi-C and Super-resolution Imaging. *Mol Cell* **59**, 588–602 (2015).
62. Wang, X. *et al.* Condensin promotes the juxtaposition of DNA flanking its loading site in Bacillus subtilis. *Genes Dev* **29**, 1661–1675 (2015).
63. Wang, X., Brandão, H. B., Le, T. B. K., Laub, M. T. & Rudner, D. Z. Bacillus subtilis SMC complexes juxtapose chromosome arms as they travel from origin to terminus. *Science* **355**, 524–527 (2017).

811 64. Hoencamp, C. *et al.* 3D genomics across the tree of life reveals condensin II as a
812 determinant of architecture type. *Science* **372**, 984–989 (2021).
813 65. Crane, E. *et al.* Condensin-driven remodelling of X chromosome topology during dosage
814 compensation. *Nature* **523**, 240–244 (2015).
815 66. Gabdank, I., Ramakrishnan, S., Villeneuve, A. M. & Fire, A. Z. A streamlined tethered
816 chromosome conformation capture protocol. *BMC Genomics* **17**, 274 (2016).
817 67. Rowley, M. J. *et al.* Analysis of Hi-C data using SIP effectively identifies loops in organisms
818 from C. elegans to mammals. *Genome Res* **30**, 447–458 (2020).
819 68. Das, M. *et al.* Condensin I folds the C. elegans genome. *bioRxiv* 2022.06.14.495661 (2022)
820 doi:10.1101/2022.06.14.495661.
821 69. C. elegans Sequencing Consortium. Genome sequence of the nematode C. elegans: a
822 platform for investigating biology. *Science* **282**, 2012–2018 (1998).
823 70. Melters, D. P., Paliulis, L. V., Korf, I. F. & Chan, S. W. L. Holocentric chromosomes:
824 convergent evolution, meiotic adaptations, and genomic analysis. *Chromosome Res.* **20**,
825 579–593 (2012).
826 71. Senaratne, A. P., Cortes-Silva, N. & Drinnenberg, I. A. Evolution of holocentric
827 chromosomes: Drivers, diversity, and deterrents. *Semin Cell Dev Biol* **127**, 90–99 (2022).
828 72. Nakagaki, M., Takei, R., Nagashima, E. & Yaginuma, T. Cell cycles in embryos of the
829 silkworm, Bombyx mori: G2-arrest at diapause stage. *Rouxs Arch Dev Biol* **200**, 223–229
830 (1991).
831 73. Rosin, L. F., Chen, D., Chen, Y. & Lei, E. P. Dosage compensation in Bombyx mori is achieved
832 by partial repression of both Z chromosomes in males. *Proc Natl Acad Sci U S A* **119**,
833 e2113374119 (2022).
834 74. Boyle, S. *et al.* The spatial organization of human chromosomes within the nuclei of
835 normal and emerin-mutant cells. *Hum Mol Genet* **10**, 211–219 (2001).
836 75. Croft, J. A. *et al.* Differences in the Localization and Morphology of Chromosomes in the
837 Human Nucleus. *J Cell Biol* **145**, 1119–1131 (1999).
838 76. Tanabe, H. *et al.* Evolutionary conservation of chromosome territory arrangements in cell
839 nuclei from higher primates. *Proc Natl Acad Sci U S A* **99**, 4424–4429 (2002).
840 77. Pontvianne, F. & Grob, S. Three-dimensional nuclear organization in Arabidopsis thaliana.
841 *J Plant Res* **133**, 479–488 (2020).
842 78. Mirny, L. & Dekker, J. Mechanisms of Chromosome Folding and Nuclear Organization:
843 Their Interplay and Open Questions. *Cold Spring Harb Perspect Biol* **14**, a040147 (2022).
844 79. Oudelaar, A. M. & Higgs, D. R. The relationship between genome structure and function.
845 *Nat Rev Genet* **22**, 154–168 (2021).
846 80. Rowley, M. J. *et al.* Condensin II Counteracts Cohesin and RNA Polymerase II in the
847 Establishment of 3D Chromatin Organization. *Cell Reports* **26**, 2890-2903.e3 (2019).
848 81. Rowley, M. J. & Corces, V. G. Organizational principles of 3D genome architecture. *Nat.*
849 *Rev. Genet.* **19**, 789–800 (2018).
850 82. Spracklin, G. *et al.* Diverse silent chromatin states modulate genome
851 compartmentalization and loop extrusion barriers. *Nat Struct Mol Biol* (2022)
852 doi:10.1038/s41594-022-00892-7.
853 83. Giaimo, B. D., Ferrante, F., Herchenröther, A., Hake, S. B. & Borggrefe, T. The histone
854 variant H2A.Z in gene regulation. *Epigenetics Chromatin* **12**, 37 (2019).
855 84. Hori, T. *et al.* Histone H4 Lys 20 monomethylation of the CENP-A nucleosome is essential
856 for kinetochore assembly. *Dev. Cell* **29**, 740–749 (2014).

857 85. Beck, D. B., Oda, H., Shen, S. S. & Reinberg, D. PR-Set7 and H4K20me1: at the crossroads
858 of genome integrity, cell cycle, chromosome condensation, and transcription. *Genes Dev*
859 **26**, 325–337 (2012).
860 86. Meyer, B. J. The X chromosome in C. elegans sex determination and dosage compensation.
861 *Curr Opin Genet Dev* **74**, 101912 (2022).
862 87. Chai, C.-L. *et al.* A genomewide survey of homeobox genes and identification of novel
863 structure of the Hox cluster in the silkworm, Bombyx mori. *Insect Biochem Mol Biol* **38**,
864 1111–1120 (2008).
865 88. Li, Z. *et al.* Genome-wide identification of polycomb target genes reveals a functional
866 association of Pho with Scm in Bombyx mori. *PLoS One* **7**, e34330 (2012).
867 89. Samejima, K. *et al.* Rules of engagement for condensins and cohesins guide mitotic
868 chromosome formation. *Science* **388**, eadq1709 (2025).
869 90. Polovnikov, K., Belan, S., Imakaev, M., Brandão, H. B. & Mirny, L. A. Fractal polymer with
870 loops recapitulates key features of chromosome organization. *bioRxiv* 2022.02.01.478588
871 (2022) doi:10.1101/2022.02.01.478588.
872 91. Nora, E. P. *et al.* Targeted Degradation of CTCF Decouples Local Insulation of Chromosome
873 Domains from Genomic Compartmentalization. *Cell* **169**, 930-944.e22 (2017).
874 92. Fudenberg, G., Abdennur, N., Imakaev, M., Goloborodko, A. & Mirny, L. A. Emerging
875 Evidence of Chromosome Folding by Loop Extrusion. *Cold Spring Harb Symp Quant Biol*
876 **82**, 45–55 (2017).
877 93. Polovnikov, K. E. *et al.* Crumpled polymer with loops recapitulates key features of
878 chromosome organization. *Phys Rev X* **13**, 041029 (2023).
879 94. Rosin, L. F., Nguyen, S. C. & Joyce, E. F. Condensin II drives large-scale folding and spatial
880 partitioning of interphase chromosomes in Drosophila nuclei. *PLoS Genet* **14**, e1007393
881 (2018).
882 95. Xiang, Y. *et al.* A molecular cell biology toolkit for the study of meiosis in the silkworm
883 Bombyx mori. *G3 (Bethesda)* **13**, jkad058 (2023).
884 96. King, T. D. *et al.* Recurrent Losses and Rapid Evolution of the Condensin II Complex in
885 Insects. *Mol Biol Evol* **36**, 2195–2204 (2019).
886 97. Rosin, L. F. *et al.* Chromosome territory formation attenuates the translocation potential
887 of cells. *Elife* **8**, e49553 (2019).
888 98. Engreitz, J. M., Agarwala, V. & Mirny, L. A. Three-dimensional genome architecture
889 influences partner selection for chromosomal translocations in human disease. *PLoS One*
890 **7**, e44196 (2012).
891 99. Xiong, K. & Ma, J. Revealing Hi-C subcompartments by imputing inter-chromosomal
892 chromatin interactions. *Nat Commun* **10**, 5069 (2019).
893 100. Johnstone, S. E. *et al.* Large-Scale Topological Changes Restrain Malignant Progression
894 in Colorectal Cancer. *Cell* **182**, 1474-1489.e23 (2020).
895 101. Vilarrasa-Blasi, R. *et al.* Dynamics of genome architecture and chromatin function
896 during human B cell differentiation and neoplastic transformation. *Nat Commun* **12**, 651
897 (2021).
898 102. Hildebrand, E. M. & Dekker, J. Mechanisms and Functions of Chromosome
899 Compartmentalization. *Trends Biochem Sci* **45**, 385–396 (2020).
900 103. Gruber, S. & Errington, J. Recruitment of condensin to replication origin regions by
901 ParB/SpoOJ promotes chromosome segregation in B. subtilis. *Cell* **137**, 685–696 (2009).

902 104. Sullivan, N. L., Marquis, K. A. & Rudner, D. Z. Recruitment of SMC by ParB-parS
903 organizes the origin region and promotes efficient chromosome segregation. *Cell* **137**,
904 697–707 (2009).
905 105. Chapard, C. *et al.* Exogenous chromosomes reveal how sequence composition drives
906 chromatin assembly, activity, folding and compartmentalization. *bioRxiv*
907 2022.12.21.520625 (2022) doi:10.1101/2022.12.21.520625.
908 106. Kim, J. *et al.* Condensin DC loads and spreads from recruitment sites to create loop-
909 anchored TADs in C. elegans. *Elife* **11**, e68745 (2022).
910 107. Rinzema, N. J. *et al.* Building regulatory landscapes reveals that an enhancer can recruit
911 cohesin to create contact domains, engage CTCF sites and activate distant genes. *Nat*
912 *Struct Mol Biol* **29**, 563–574 (2022).
913 108. Tjalsma, S. J. D. *et al.* H4K20me1 and H3K27me3 are concurrently loaded onto the
914 inactive X chromosome but dispensable for inducing gene silencing. *EMBO Rep* **22**, e51989
915 (2021).
916 109. Senaratne, A. P. *et al.* Formation of the CenH3-Deficient Holocentromere in
917 Lepidoptera Avoids Active Chromatin. *Curr Biol* **31**, 173-181.e7 (2021).
918 110. Rekaik, H. & Duboule, D. A CTCF-dependent mechanism underlies the Hox timer:
919 relation to a segmented body plan. *Curr Opin Genet Dev* **85**, 102160 (2024).
920

Figure 1

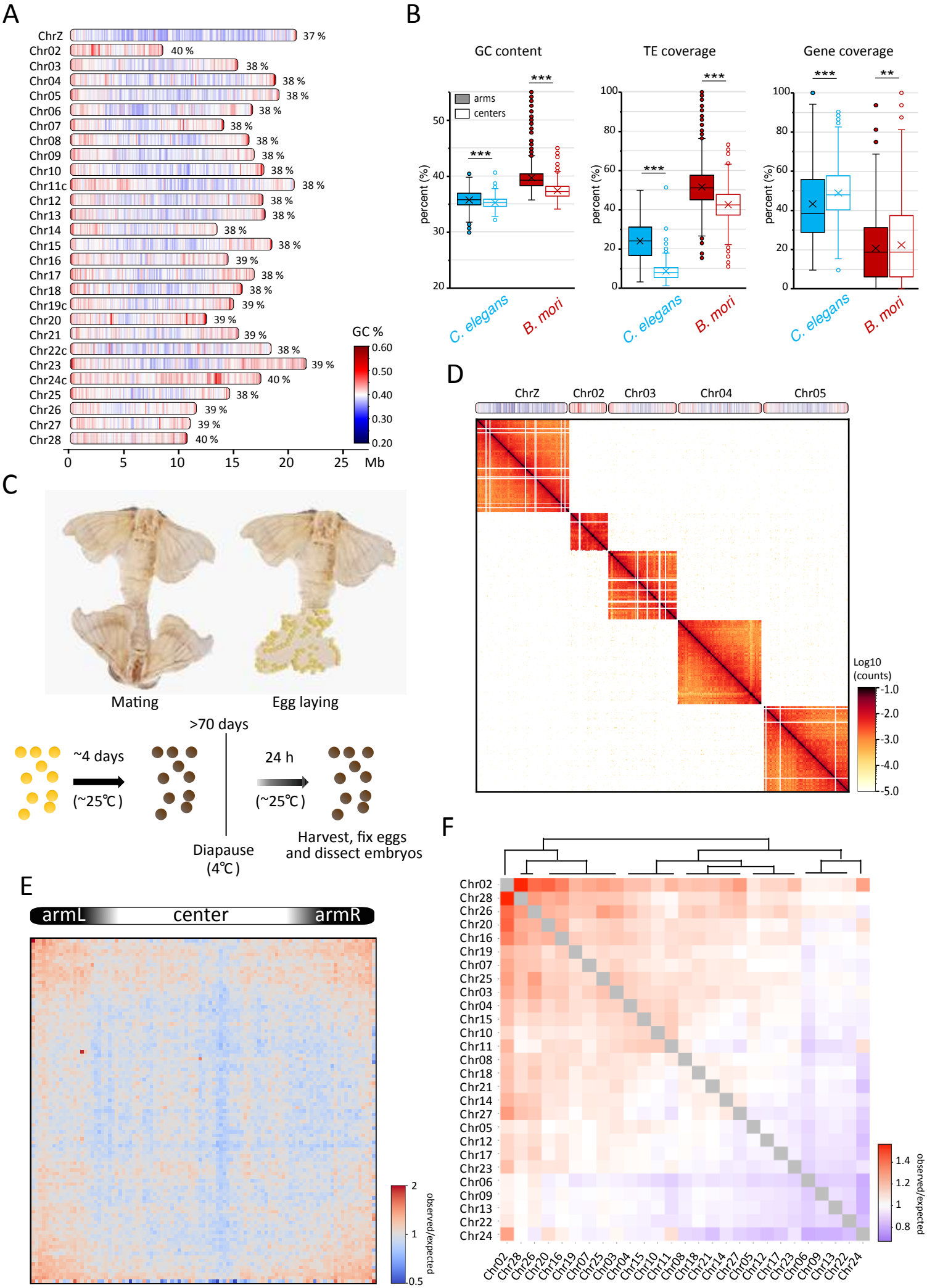
A
ChrZ 37 %
Chr02 40 %
Chr03 38 %
Chr04 38 %
Chr05 38 %
Chr06 38 %
Chr07 38 %
Chr08 38 %
Chr09 38 %
Chr10 38 %
Chr11c 38 %
Chr12 38 %
Chr13 38 %
Chr14 38 %
Chr15 38 %
Chr16 39 %
Chr17 38 %
Chr18 38 %
Chr19c 39 %
Chr20 39 %
Chr21 39 %
Chr22c 38 %
Chr23 39 %
Chr24c 40 %
Chr25 38 %
Chr26 39 %
Chr27 39 %
Chr28 40 %
GC %
0.60
0.50
0.40
0.30
0.20
0 5 10 15 20 25 Mb
B
GC content
TE coverage
Gene coverage
arms
centers
percent (%)
***
**
C. elegans
B. mori
C
Mating
Egg laying
>70 days
~4 days
(~25℃)
24 h
(~25℃)
Diapause
(4℃)
Harvest, fix eggs
and dissect embryos
D
ChrZ
Chr02
Chr03
Chr04
Chr05
Log10
(counts)
-1.0
-2.0
-3.0
-4.0
-5.0
E
armL
center
armR
2
1
0.5
observed/expected
F
Chr02
Chr28
Chr26
Chr20
Chr16
Chr19
Chr07
Chr25
Chr03
Chr04
Chr15
Chr10
Chr11
Chr08
Chr18
Chr21
Chr14
Chr27
Chr05
Chr12
Chr17
Chr23
Chr06
Chr09
Chr13
Chr22
Chr24
1.4
1.2
1
0.8
observed/expected

<u>Figure 1</u>: Hi-C of *Bombyx mori* embryos reveals highly distinct chromosome territories.

(**A**) Schematics of *B. mori* chromosomes drawn to approximate scale indicated in Mb below. For each chromosome, total GC content in percentage is noted, and local GC content per 100 kb windows is indicated as a color scale from blue (<20%) to red (>60%). A suffix "c" added to a chromosome's name indicates assembly corrections were made (Figure S9). (**B**) Box plots showing the distribution of GC content, TE coverage, and gene density per 100 kb window in center and arm regions of autosomes in *C. elegans* and *B. mori*. Statistical significance was tested using a Mann-Whitney U-test, **: P-value < 0.05, ***: P-value < 0.005. Box region corresponds to data between the first and third quartile. Lines indicate medians of respective distributions, while crosses correspond to their means. Whiskers extend to the lowest and highest data points, excluding outliers, which are shown as dots. (**C**) Sample generation for Hi-C and ChIP-Seq. (**D**) Contact map at 80 kb bin resolution of five selected *B. mori* chromosomes (*on top*). (**E**) Average inter-chromosomal (*trans*) $^{observed}/_{expected}$ matrix for all scaled *B. mori* chromosomes, computed at 40 kb bin resolution. (**F**) Heatmap illustrating $^{observed}/_{expected}$ inter-chromosomal contact frequencies as a divergent color scale from blue to red. Chromosomes have been clustered and ordered to reflect similar contact patterns.

Figure 2

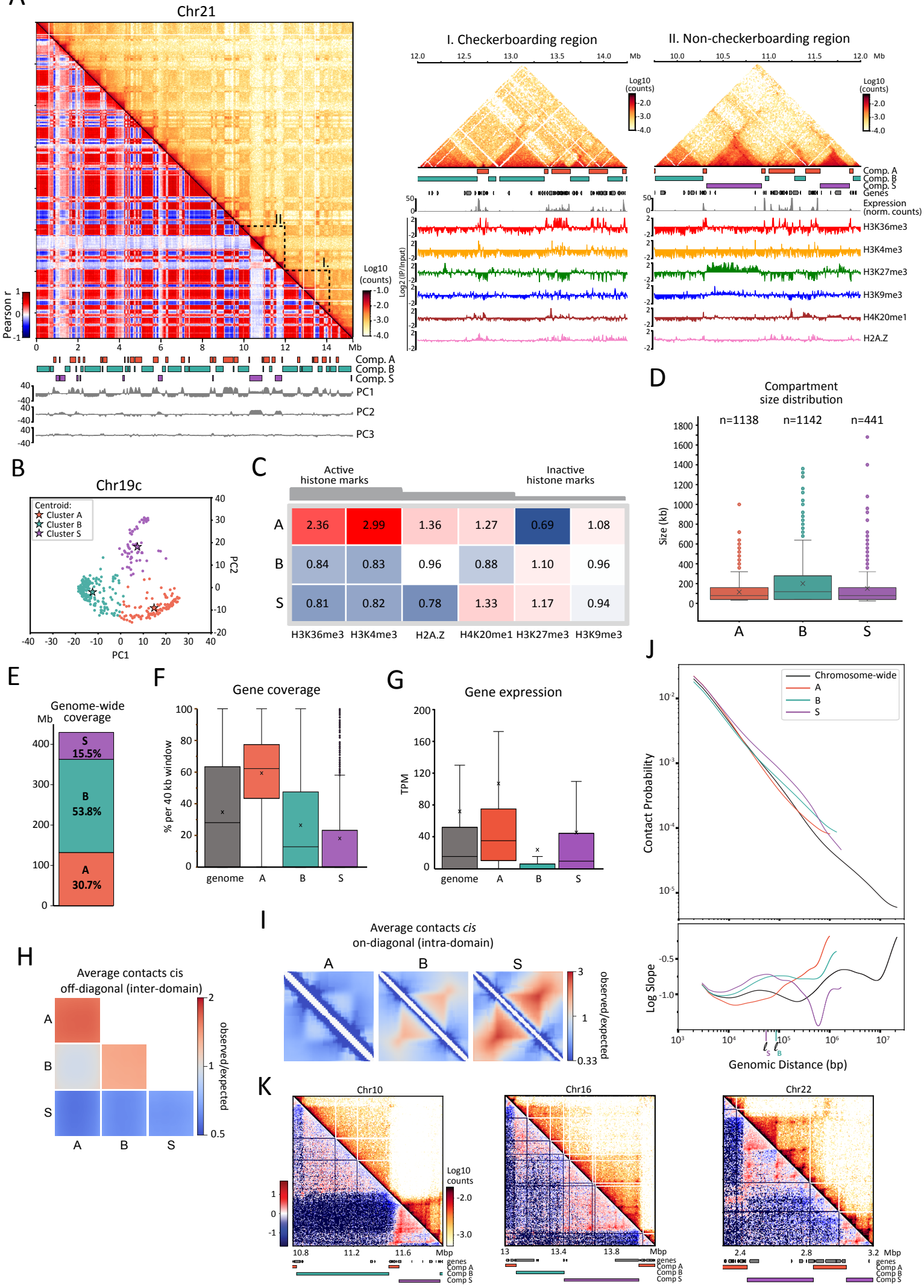
A
Chr21
Pearson r
Log10 (counts)
Mb
Comp. A
Comp. B
Comp. S
PC1
PC2
PC3
I. Checkerboarding region
II. Non-checkerboarding region
Log2 (IP/Input)
Genes
Expression (norm. counts)
H3K36me3
H3K4me3
H3K27me3
H3K9me3
H4K20me1
H2A.Z
B
Chr19c
Centroid:
Cluster A
Cluster B
Cluster S
PC1
PC2
C
Active histone marks
Inactive histone marks
A 2.36 2.99 1.36 1.27 0.69 1.08
B 0.84 0.83 0.96 0.88 1.10 0.96
S 0.81 0.82 0.78 1.33 1.17 0.94
H3K36me3 H3K4me3 H2A.Z H4K20me1 H3K27me3 H3K9me3
D
Compartment size distribution
n=1138 n=1142 n=441
Size (kb)
A B S
E
Genome-wide coverage
Mb
S 15.5%
B 53.8%
A 30.7%
F
Gene coverage
% per 40 kb window
genome A B S
G
Gene expression
TPM
genome A B S
J
Chromosome-wide
A
B
S
Contact Probability
Log Slope
Genomic Distance (bp)
H
Average contacts cis off-diagonal (inter-domain)
observed/expected
A B S
I
Average contacts cis on-diagonal (intra-domain)
A B S
observed/expected
K
Chr10
Chr16
Chr22
Log10 counts
Mbp
genes
Comp A
Comp B
Comp S

<u>Figure 2</u>: Hi-C compartment analysis reveals a novel and secluded chromatin folding structure

(**A**) *Left*: top diagonal represents the iterative-corrected Hi-C contact map of Chr21 at 40 kb bin resolution, and bottom diagonal is the corresponding Pearson correlation matrix. Below the matrix are the gene track (black), color boxes indicating the locations of domains of compartment A (orange), B (turquoise), and S (purple) and tracks of the first three principal components (gray) computed from the correlation matrix. *Right*: close-up on regions highlighted on the left, I: checkerboarding region, II: non-checkerboarding region. Below matrices are tracks for compartments and genes as in the left as well as corresponding RNA-seq at 1 kb resolution and ChIP-Seq tracks for various histone marks at 25 bp resolution. (**B**) Example of clustering along PC1 and PC2 of Pearson correlation matrix for Chr19c. Clusters called using k-means function of scikit-learn are shown in different colors. For each cluster, the centroid and the corresponding assignment to A, B, and S compartments is indicated. (**C**) Heatmap showing genome-wide enrichment of assayed histone marks across compartment A, B, and S. Enrichment values correspond to median of IP/input ratios at 40 kb resolution normalized to the genome-wide median for each mark. (**D**) Box plots showing the size distribution of A, B, and S domains. Boxed regions correspond to data between the first and third quartile. Lines indicate the medians of respective distributions, while crosses correspond to their means. Whiskers extend to the lowest and highest data points, excluding outliers, shown by dots. (**E**) Bar graph showing relative genomic coverage of A, B, and S. (**F**) Box plots showing distribution of gene coverage per 40 kb window of the whole genome (n = 11,143) or within A (n = 3,294), B (n = 5,772), and S (n = 1,670). Line indicates median of distribution while cross corresponds to mean. Whiskers extend to lowest and highest data points, excluding outliers, which have been removed. All distributions in each compartment for all features are significantly different from each other and from the genome-wide distribution by the Mann-Whitney (95%, two-tailed) U-test. (**G**) Box plots showing range of gene expression (in TPM) (whole genome: n = 13,869, in A: n = 7,404, in B: n = 4,500, in S: n = 608). (**H**) Average *cis* off-diagonal (inter-domain) $^{observed}/_{expected}$ contact enrichment plots (log scale) within and between all rescaled A, B, and S compartments. (**I**) Rescaled average *cis* on-diagonal (intra-domain) $^{observed}/_{expected}$ contact enrichments (log scale) for the three compartment types. (**J**) *Top:* Contact probability as a function of genomic distance, P(*s*), curve for the PD-D2 Hi-C data (*s*). *Bottom*: Log-derivative of contact probability as a function of genomic distance. Curves represent averages of either chromosome-wide (gray) or for contiguous segments of a given compartment type (colored). Estimates of the average loop size in S (ℓ_S) and in B (ℓ_B), corresponding to the peaks in the log-derivative curves, are labeled on the x-axis. (**K**) Regions of the PD-D2 Hi-C maps (top diagonal) along with the corresponding Pearson correlation matrix (bottom diagonal) displaying characteristic features of loop extrusion at 5 kb resolution, with compartment and gene tracks below.

Figure 3

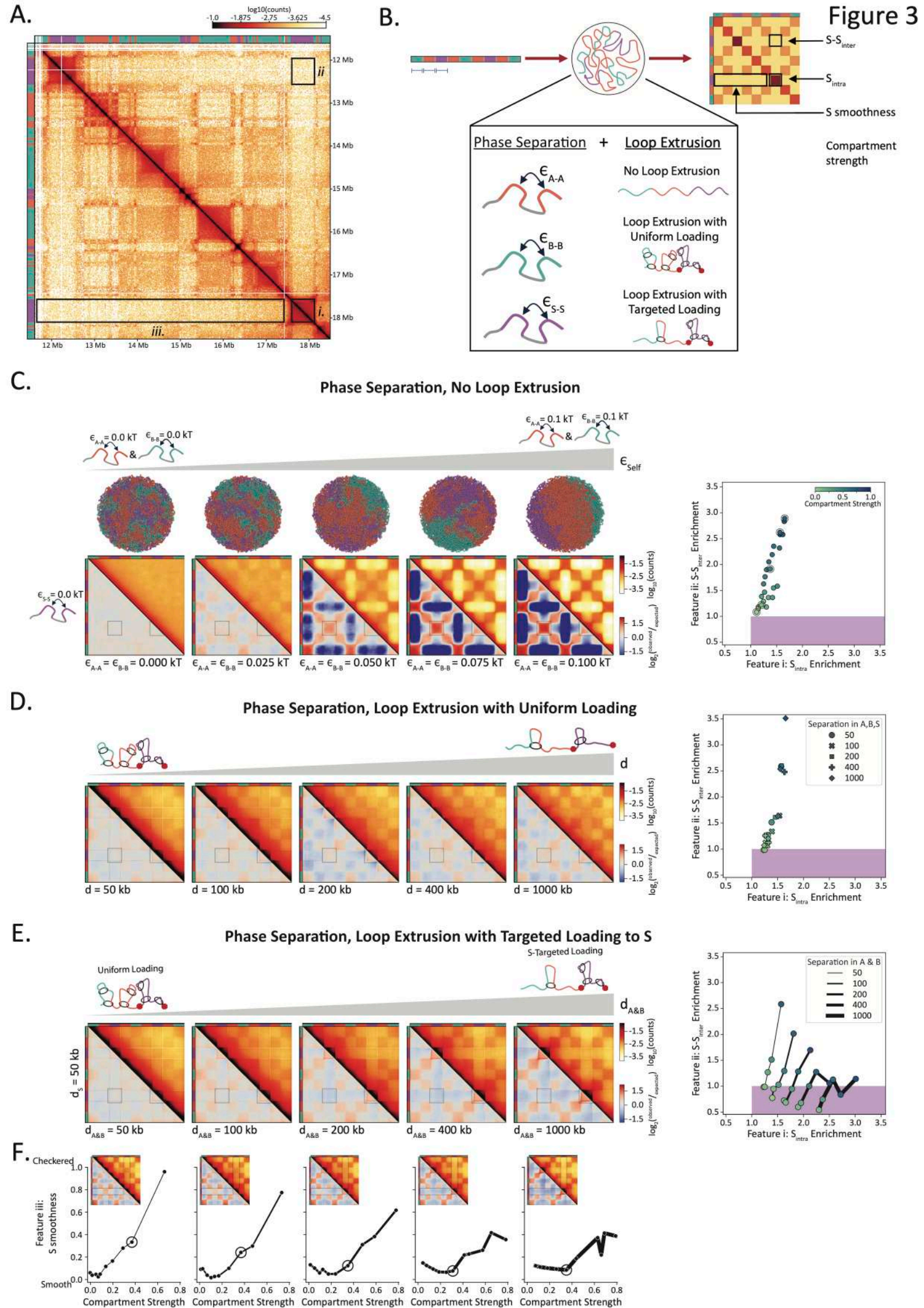
A.
log10(counts)
-1.0 -1.875 -2.75 -3.625 -4.5
12 Mb
13 Mb
14 Mb
15 Mb
16 Mb
17 Mb
18 Mb
i.
ii
iii.
B.
S-S inter
S intra
S smoothness
Compartment strength
Phase Separation + Loop Extrusion
ϵA-A
ϵB-B
ϵS-S
No Loop Extrusion
Loop Extrusion with Uniform Loading
Loop Extrusion with Targeted Loading
C.
Phase Separation, No Loop Extrusion
ϵA-A = 0.0 kT
ϵB-B = 0.0 kT
ϵA-A = 0.1 kT
ϵB-B = 0.1 kT
ϵSelf
ϵS-S = 0.0 kT
log10(counts)
log2(observed/expected)
ϵA-A = ϵB-B = 0.000 kT
ϵA-A = ϵB-B = 0.025 kT
ϵA-A = ϵB-B = 0.050 kT
ϵA-A = ϵB-B = 0.075 kT
ϵA-A = ϵB-B = 0.100 kT
Compartment Strength
Feature ii: S-S inter Enrichment
Feature i: S intra Enrichment
D.
Phase Separation, Loop Extrusion with Uniform Loading
d
d = 50 kb
d = 100 kb
d = 200 kb
d = 400 kb
d = 1000 kb
Separation in A,B,S
50
100
200
400
1000
E.
Phase Separation, Loop Extrusion with Targeted Loading to S
Uniform Loading
S-Targeted Loading
dA&B
ds = 50 kb
dA&B = 50 kb
dA&B = 100 kb
dA&B = 200 kb
dA&B = 400 kb
dA&B = 1000 kb
Separation in A & B
F.
Checkered
Smooth
Feature iii: S smoothness
Compartment Strength

<u>Figure 3</u>: Mechanistic polymer modeling reveals S chromatin organization can arise from targeted loop extrusion in S chromatin but not from other known genome folding mechanisms.

(**A**) Hi-C map and sub-compartment annotations highlighting the three distinct features of S compartments: *i*) on-diagonal contact enrichment within S domains, *ii*) off-diagonal contact depletion between different S domains, and *iii*) smooth depletion of contacts between S and the rest of the chromosome. Hi-C data corresponds to chromosome 22: 11,625,000-18,435,000 from PD-D2 samples mapped with distiller (see Methods). (**B**) Illustration of the approach to testing different mechanistic models of S compartment formation. Polymer segments are assigned to compartments A, B, or S, which specifies their pairwise affinities. One model without loop extrusion and two models with loop extrusion are considered. Simulations are evaluated based on whether their contact maps display features *i*, *ii*, and *iii*. Compartment strength is also measured. (**C**) Three-species phase separation modeling results. *Left*: sampled conformations and corresponding Hi-C maps of chromosome models with increasing phase separation driven by increasing both A-A and B-B affinities, $\epsilon_{A\text{-}A}$ and $\epsilon_{B\text{-}B}$ (from left to right). *Right*: scatter plot of $^{observed}/_{expected}$ contact enrichments of S features *i* and *ii* for all simulated A-to-A and B-to-B affinities. Purple boxed region reflects the broadest value range for S-like features. Data points corresponding to chromosome models shown on the left are circled in the scatter plot. (**D**) Phase separation and uniform loop extrusion with barriers modeling results. *Left:* Hi-C maps of models with increasing chromosome-wide separation, d, of loop extruders. Phase separation was induced in all maps on the left by setting $\epsilon_{A\text{-}A} = \epsilon_{B\text{-}B} = 0.05$ kT. *Right:* scatter plot of $^{observed}/_{expected}$ contact enrichments of S features *i* and *ii* for models varying in extruder separations, A-A, and B-B affinities, with points colored by compartment strength as in (**C**). For all models shown, processivity was fixed to 100 kb and S-to-S affinity, $\epsilon_{S\text{-}S}$, set to 0.0 kT. (**E**) Phase separation and loop extrusion with targeted loading to S modeling results. *Left*: Hi-C maps of models with increasing separation of loop extruders in A and B ($d_{A\&B}$), while extruder separation in S (d_S) was fixed at 50 kb. Phase separation was induced in all maps on the left by setting $\epsilon_{A\text{-}A} = \epsilon_{B\text{-}B} = 0.05$ kT. *Right*: scatter plot of $^{observed}/_{expected}$ contact enrichments of S features *i* and *ii* for a range of A-to-A and B-to-B affinities and separations in A and B ($d_{A\&B}$), with d_S fixed to 50 kb. Data points sharing $d_{A\&B}$ (i.e. varying $\epsilon_{A\text{-}A}$ and $\epsilon_{B\text{-}B}$) were connected by line, with the value of $d_{A\&B}$ reflected in line thickness. The line corresponding to $d_{A\&B} = 50$ kb reflects the uniform loading scenario. (**F**) Impact of S-targeted extruder loading on the smoothness of S compartment contact depletion (feature *iii*). Smoothness was computed as the standard deviation of mean observed/expected S-A, S-B, and S-S_{inter} contacts, with lower y values corresponding to smoother compartment patterning. Data points with compartment strengths of approximately 0.4 are circled and corresponding Hi-C maps are shown in the insets. Separation in S (d_S) was fixed at 50 kb.

Figure 4

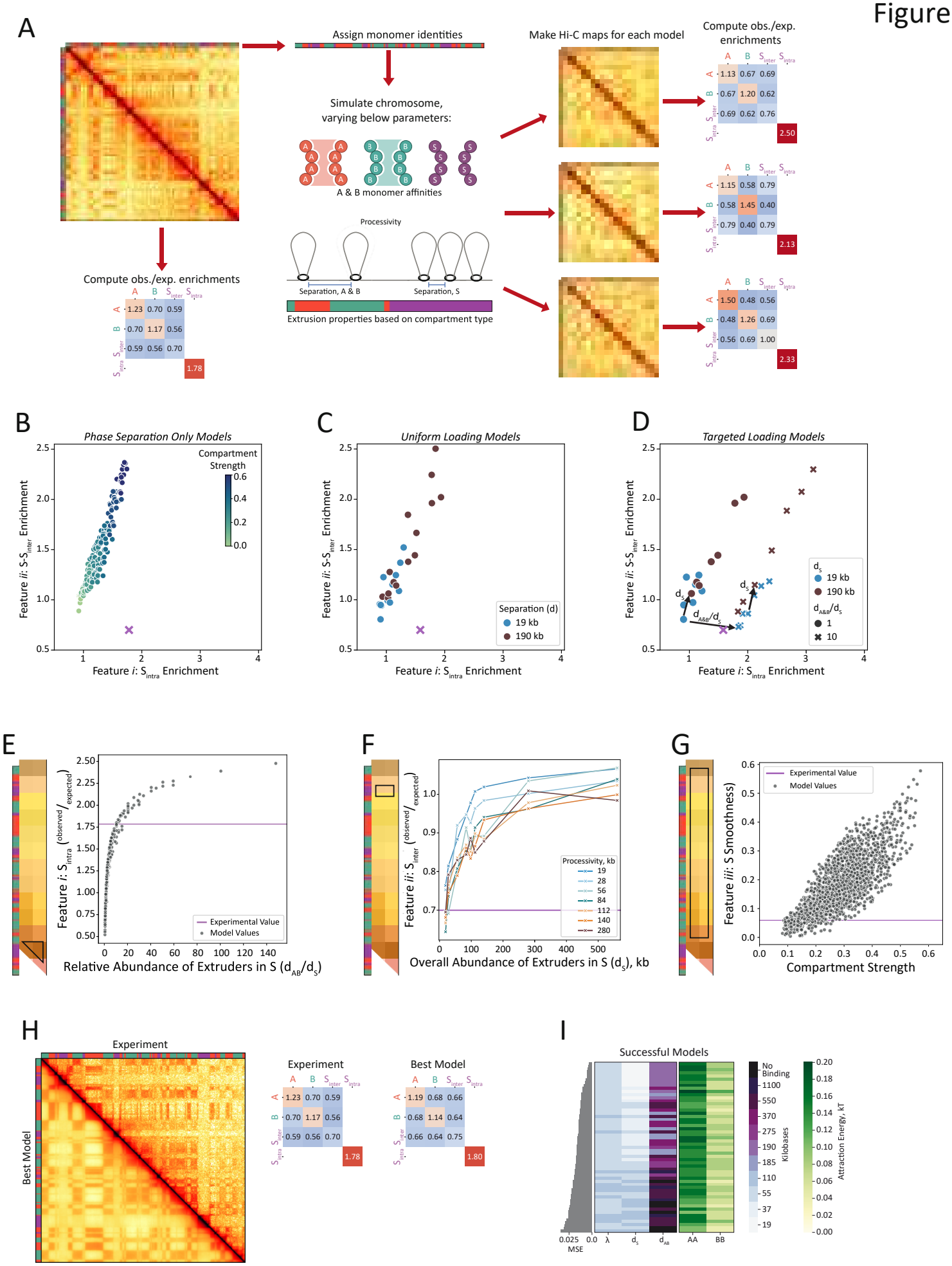
A
Assign monomer identities
Simulate chromosome, varying below parameters:
A & B monomer affinities
Processivity
Separation, A & B
Separation, S
Extrusion properties based on compartment type
Make Hi-C maps for each model
Compute obs./exp. enrichments
Compute obs./exp. enrichments
B
Phase Separation Only Models
Compartment Strength
Feature ii: S-S_inter Enrichment
Feature i: S_intra Enrichment
C
Uniform Loading Models
Separation (d)
19 kb
190 kb
D
Targeted Loading Models
d_s
19 kb
190 kb
d_AB/d_s
1
10
E
Experimental Value
Model Values
Relative Abundance of Extruders in S (d_AB/d_s)
F
Processivity, kb
Overall Abundance of Extruders in S (d_s), kb
G
Experimental Value
Model Values
Feature iii: S Smoothness
Compartment Strength
H
Experiment
Best Model
I
Successful Models
No Binding
Kilobases
Attraction Energy, kT
MSE

<u>Figure 4</u>: Chromosome-scale polymer modeling reveals how different features of S arise

(**A**) Approach to generating chromosomal polymer models of *B. mori*. Locus corresponds to chromosome 15: 0-6,500,000 mapped with distiller (see Methods). Polymer segments are assigned to compartments A, B, or S based on sub-compartment assignments of the region. Simulations are performed for three different phase separation and/or extrusion models. $^{Observed}/_{expected}$ contact enrichments are computed for different intra- and inter-compartment interactions for comparison to the experimental Hi-C data. (**B**) Scatter plot of $^{observed}/_{expected}$ contact enrichments of S features *i* and *ii* from chromosome-scale polymer modeling of three-species phase separation and no loop extrusion over a range of different A-to-A and B-to-B affinities. The corresponding S_{intra} and S-S_{inter} values from chromosome 15: 0-6,500,000 of the PD-D2 Hi-C data are shown as a purple x. (**C**) Scatter plot of $^{observed}/_{expected}$ contact enrichments of S features *i* and *ii* from chromosome-scale polymer modeling of three-species phase separation and loop extrusion with uniform loading for two different separations, d = 19 or 190 kb, and two processivities, λ = 19 and 190 kb, over a range of A-to-A and B-to-B affinities and extrusion processivities. (**D**) Scatter plot of $^{observed}/_{expected}$ contact enrichments of S features *i* and *ii* from chromosome-scale polymer modeling of three-species phase separation and loop extrusion with targeted loading to S for two different d_S and $d_S/d_{A\&B}$ ratios over a range of different interaction affinities. (**E**) $^{Observed}/_{expected}$ contact enrichments of S_{intra} plotted as a function of relative abundance of loop extruders ($d_{A\&B}/d_S$) for a series of chromosome models with λ, d_S, and $d_{A\&B}$ varied. The experimental value of S_{intra} is shown as a purple line. A-to-A and B-to-B affinities were fixed at 0.12 and 0.04 kT, respectively. (**F**) $^{Observed}/_{expected}$ values of S-S_{inter} plotted as a function of separation between loop extruders in S (d_S) for a series of chromosome models. Each curve represents a series of models, which share loop extruder processivity. All models lacked extrusion in A and B chromatin and shared homotypic attractions of $\epsilon_{A\text{-}A}$ = 0.12, $\epsilon_{B\text{-}B}$ = 0.04, and $\epsilon_{S\text{-}S}$ = 0.00 kT, to yield an A/B compartment strength similar to that observed in the experimentally generated PD-D2 Hi-C maps. The experimentally measured value of S-S_{inter} is shown as a purple line. (**G**) S compartment smoothness plotted as a function of compartment strength. Simulations varied in $\epsilon_{A\text{-}A}$, $\epsilon_{B\text{-}B}$, λ, d_S, and $d_{A\&B}$. Smoothness was computed as the standard deviation of $^{observed}/_{expected}$ S-A, S-B, and S-S_{inter} contacts. The experimentally measured value of S smoothness from the PD-D2 maps is shown as a purple line. (**H**) Comparison of the experimental data for chromosome 15: 0-6,500,000 (mapped with distiller) versus the best polymer model ($\epsilon_{A\text{-}A}$ = 0.16 kT, $\epsilon_{B\text{-}B}$ = 0.08 kT, $\epsilon_{S\text{-}S}$ = 0.00 kT, λ = 55 kb, d_S = 19 kb, $d_{A\&B}$ = 190 kb). *Left:* Experimentally generated Hi-C (*top, right half of the map*) versus the *in silico* generated Hi-C map from the best model (*bottom, left half of the map*). *Right*: Summary statistics ($^{observed}/_{expected}$ off-diagonal compartment and on-diagonal S_{intra} enrichments) for the experimentally generated data (*left*) and best model (*right*). (**I**) Parameter values for extruder properties (*left*) and homotypic A-to-A and B-to-B affinities (*right*) of the successful models, sorted by rank of their mean square error of their summary statistics compared to those of the experimental data. All models lacked S-to-S affinities.

Figure 5

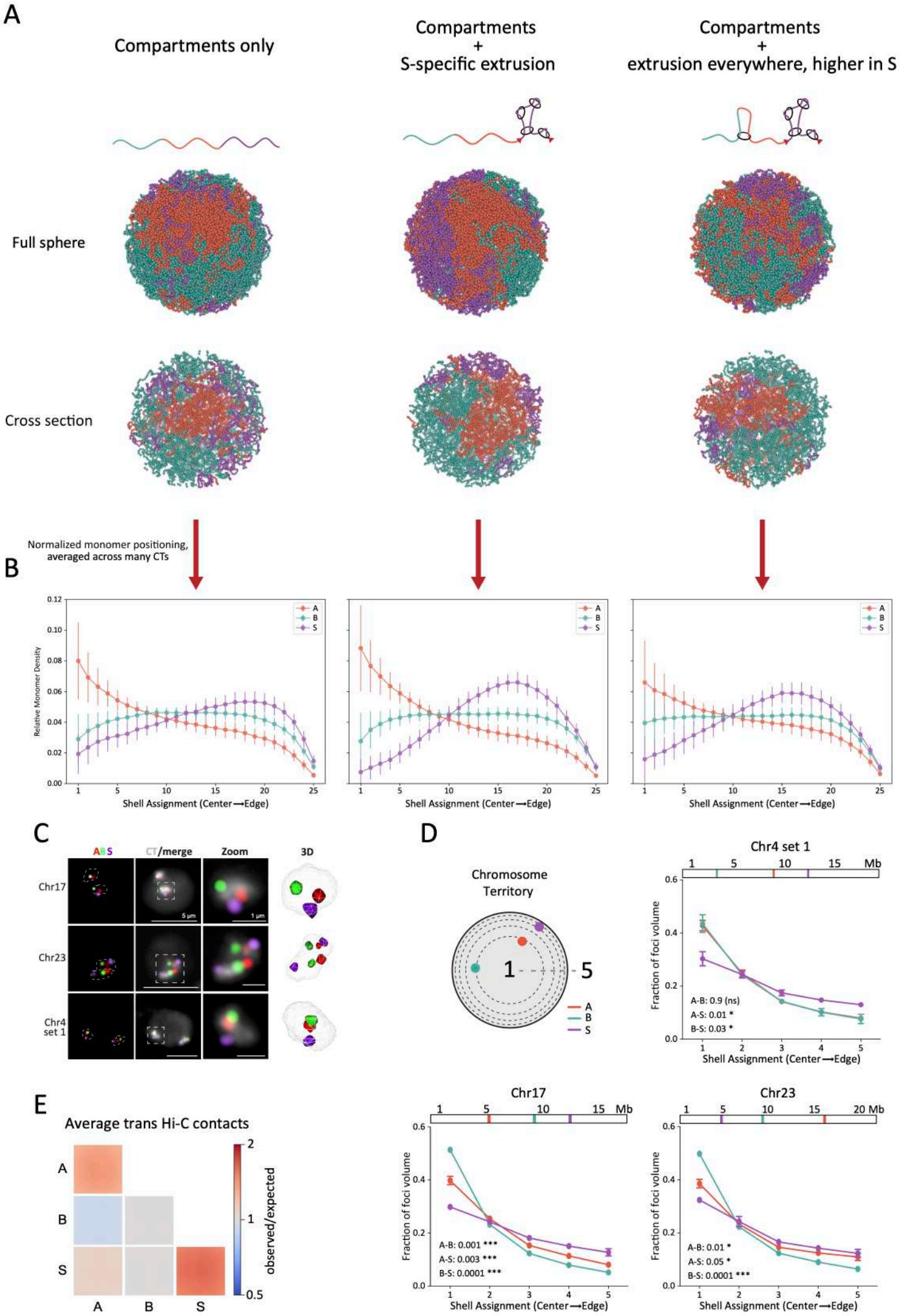
A
Compartments only
Compartments + S-specific extrusion
Compartments + extrusion everywhere, higher in S
Full sphere
Cross section
Normalized monomer positioning, averaged across many CTs
B
Relative Monomer Density
Shell Assignment (Center→Edge)
A
B
S
C
A B S
CT/merge
Zoom
3D
Chr17
Chr23
Chr4 set 1
5 µm
1 µm
D
Chromosome Territory
1
5
Chr4 set 1
Mb
Fraction of foci volume
A-B: 0.9 (ns)
A-S: 0.01 *
B-S: 0.03 *
E
Average trans Hi-C contacts
observed/expected
Chr17
A-B: 0.001 ***
A-S: 0.003 ***
B-S: 0.0001 ***
Chr23
A-B: 0.01 *
A-S: 0.05 *
B-S: 0.0001 ***

<u>Figure 5</u>: Compartment S is peripherally located within chromosome territories, with modeling indicating a role for loop extrusion in this positioning.

(**A**) Example conformations for three models of chromosome 15, with the top row's renderings reflecting the entire spherically confined simulation and the bottom row's renderings representing cross sections through the center of the sphere. Each column represents a model introducing a new source of organization to the chromosome; (*left*) a rendering of a phase-separation-only model ($\epsilon_{A\text{-to-}A}$ = 0.16 kT, $\epsilon_{B\text{-to-}B}$ = 0.08 kT, $\epsilon_{S\text{-to-}S}$ = 0.00 kT); (*middle*) a rendering of the same compartment model with loop extrusion within S only (λ = 55 kb, d_S = 19 kb); (*right*) a rendering of the same compartment model as the far left but with different loop extruder separations in S versus A and B (λ = 55 kb, d_S = 19 kb, d_{AB} = 190 kb; the best model from the previous section). (**B**) Relative monomer densities for A, B, and S monomers for the three models detailed in Panel 5A. (**C**) Four-color Oligopaint FISH labeling single A (red), B (green), and S (purple) domains as well as the corresponding CT (white). *First column*: Oligopaint labeling of domains, with white dashed lines indicating CT edges. *Second column*: Oligopaint labeling of domains merged with Oligopaint labeling of CTs. *Third column*: zoom-in views corresponding to boxes traced in column two. *Fourth column*: 3D rendering of zoomed CT from TANGO [91]. Microscope images are Z projections of 10 Z stacks. The background in the CT channel acts as a proxy for the nuclear edge. (**D**) Shell analysis measuring compartment foci positions within their CTs for Chr04, 17, and 23. The location of Oligopaint FISH probes within the chromosome is shown above each plot. Dots indicate means of 3 biological replicates (different embryos, n > 250 nuclei). Error bars show standard error of the mean. P-values were generated from unpaired t-test (Kolmogorov-Smirnov test) between distributions and are indicated at the bottom left of each graph. (**E**) Average $^{observed}/_{expected}$ *trans* (inter-chromosomal) contacts within and between all A, B, and S compartments.

Figure 6

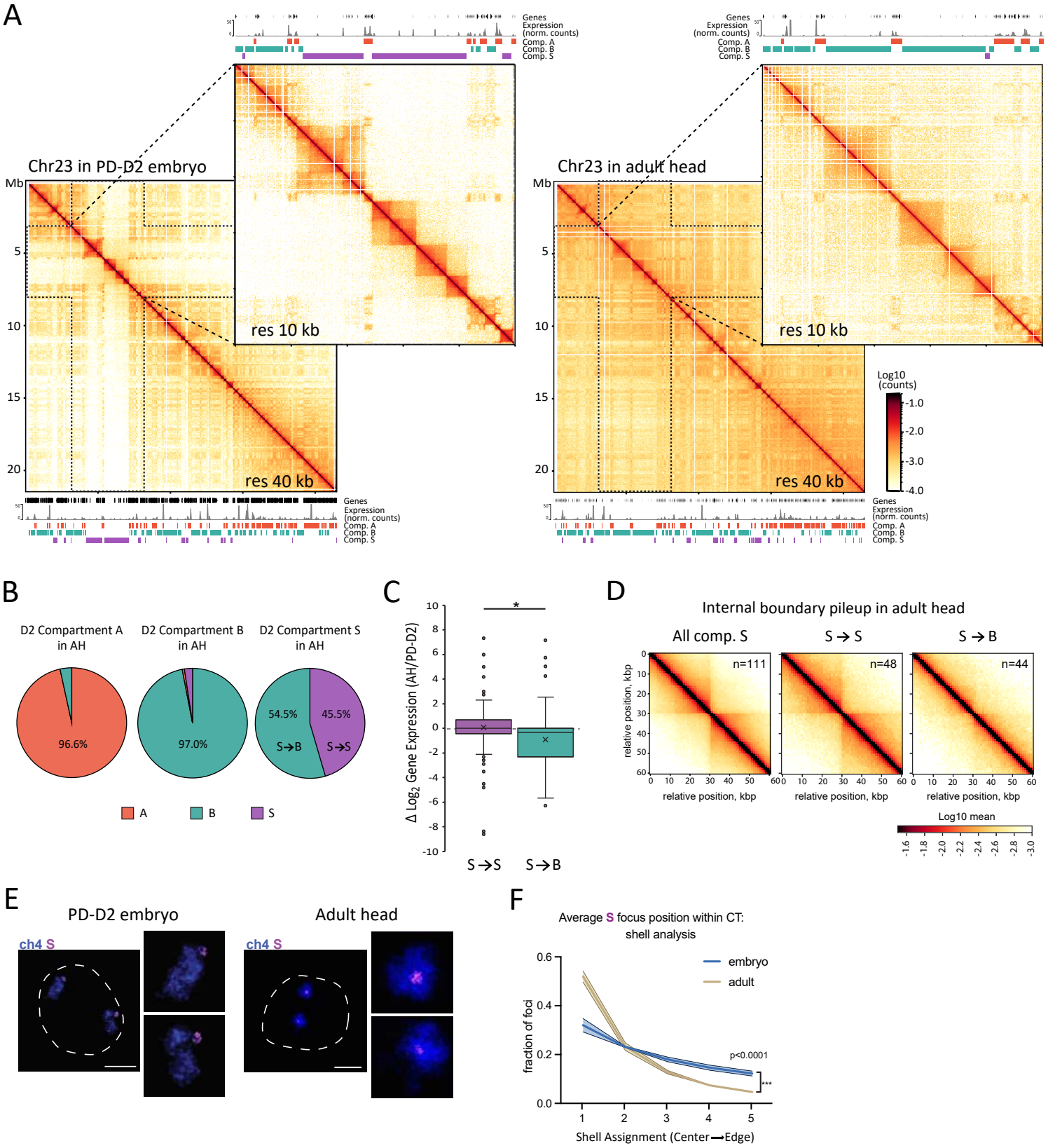
A
Chr23 in PD-D2 embryo
Chr23 in adult head
Mb
res 10 kb
res 40 kb
Genes
Expression (norm. counts)
Comp. A
Comp. B
Comp. S
Log10 (counts)
B
D2 Compartment A in AH
D2 Compartment B in AH
D2 Compartment S in AH
96.6%
97.0%
54.5%
45.5%
S→B
S→S
A
B
S
C
Δ Log2 Gene Expression (AH/PD-D2)
S→S
S→B
D
Internal boundary pileup in adult head
All comp. S
S → S
S → B
n=111
n=48
n=44
relative position, kbp
Log10 mean
E
PD-D2 embryo
Adult head
ch4 S
F
Average S focus position within CT: shell analysis
embryo
adult
fraction of foci
p<0.0001
Shell Assignment (Center→Edge)

<u>Figure 6</u>: Compartment S changes during development.

(**A**) Hi-C contact maps of the full Chr23 at 40 kb resolution and Chr23:3,000,000-80,000,00 region at 10 kb resolution in PD-D2 embryos on the left and in adult head (AH) on the right. Below or above each matrix are gene locations, RNA-seq expression aggregated at 1 kb resolution and compartments A, B, and S assignments, for the corresponding stage and region. (**B**) Compartment assignment in AH datasets of large domains (>200 kb) assigned to large compartment A, B, or S in PD-D2, in % of the compartments assigned in PD-D2. (**C**) Box plots of distributions of $\log_2$ ratio of gene expression (TPM) between PD-D2 embryos and AH. In purple is the distribution for genes that are in domains assigned to compartment S in the two stages (S→S) (n=119), and in green is the distribution for genes that are in region assigned to compartment S in PD-D2 and that switched to B in AH (S→B) (n = 120). Boxed region corresponds to data between first to third quartile. Line indicates median of distribution while cross corresponds to mean. Whiskers extend to lowest and highest non-outlier data points, and dots outside correspond to outliers. Asterisks indicate distributions significantly different by Kolmogorov-Smirnov test (*: P-value = 0.01 - 0.05). (**D**) Pileup plots centered on internal insulation points within all large S compartment domains (>200 kb, excluding 40 kb on each side of domain boundaries) in AH or S→S and S→B categories, as described in the right panel of (B), at 5 kb resolution and extending to 30 kb on each side. (**E**) Two-color STED labeling chr04 CT and single S domain in cells from PD-D2 embryos (left) or adult heads (right). Chr04 is shown in blue, and the S compartment domain is shown purple. Dashed line indicates nuclear edge as determine by confocal microscopy**.** (**F**) Shell analysis measuring S domain positions within Chr04 in embryos (blue) and adult heads (tan). Mid line = average of 2-3 biological replicates (n>30 nuclei each). Error bars (light shading) show standard error of the mean. P-values were generated from unpaired t-tests (Kolmogorov-Smirnov tests) between distributions and are indicated at the bottom right of the graph.

Table 1: **Molecular Function enrichment of *B.mori* genes in S.**

Pathway	GO ID	Enrichment FDR	Number of genes in category	Total number of pathway genes	Fold Enrichment
DNA binding	GO:0003677	6.10E-23	66	592	4.45
Nucleic acid binding	GO:0003676	7.43E-14	89	1461	2.43
DNA-binding transcription factor activity	GO:0003700	3.18E-13	31	220	5.63
Transcription regulator activity	GO:0140110	5.13E-12	32	262	4.88
Sequence-specific DNA binding	GO:0043565	7.10E-08	19	139	5.46
DNA-binding transcription factor activity, RNA polymerase II-specific	GO:0000981	2.811E-06	13	80	6.49
Nuclear receptor activity	GO:0004879	4.05E-03	4	12	13.32
Ligand-activated transcription factor activity	GO:0098531	4.05E-03	4	12	13.32
Steroid hormone receptor activity	GO:0003707	1.22E-02	4	16	9.99
Signaling receptor binding	GO:0005102	2.77E-02	7	67	4.17